STUDIA UNIVERSITATIS
BABEŞ-BOLYAI

Volume 70, No. 1 (2025)

Engineering

UNIVERSITATEA BABEŞ-BOLYAI
BABEŞ-BOLYAI TUDOMÁNYEGYETEM
BABEŞ-BOLYAI UNIVERSITÄT
BABEŞ-BOLYAI UNIVERSITY
TRADITIO ET EXCELLENTIA

STUDIA UNIVERSITATIS
BABEŞ-BOLYAI
www.studia.ubbcluj.ro
51 B.P. Hasdeu Street, 400371
Cluj-Napoca, ROMANIA

CLUJ UNIVERSITY PRESS
www.editura.ubbcluj.ro

ISSN: 2734-7680
ISSN-L: 2734-7680

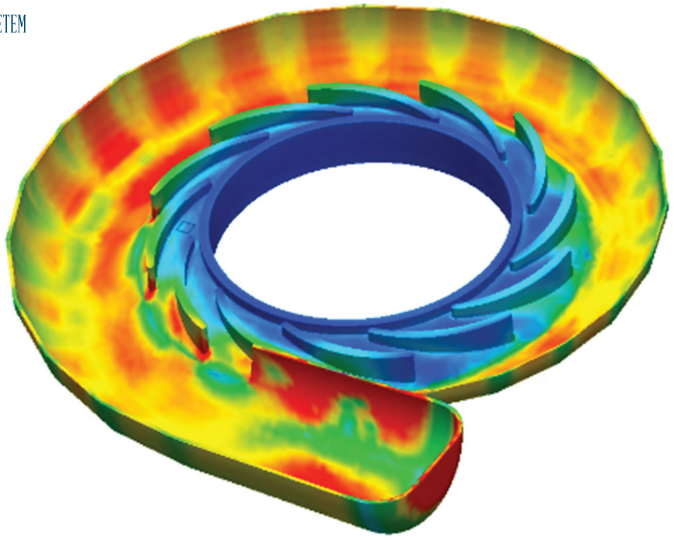

Studia Universitatis Babeş-Bolyai
ENGINEERING

The Journal of the Faculty of Engineering at Reşiţa

Babeş-Bolyai University from Cluj-Napoca

Volume 70, No. 1, 2025

doi:10.24193/subbeng.2025.1

Published Online: 2025-12-20

ISSN (Online): 2734-7680

EDITORIAL OFFICE:

Piața Traian Vuia, Nr. 1-4, 320085, Reșița,
Caraș-Severin, România
https://studia.reviste.ubbcluj.ro/index.php/subbengineering/

PUBLISHER: BABEŞ-BOLYAI UNIVERSITY

B.P. Hasdeu str. no. 51, 400371 Cluj-Napoca, Romania
Phone: +40-264-405300 *6452; Fax: +40-264-591906
e-mail: studiaubb@ubbcluj.onmicrosoft.com

STUDIA UNIVERSITATIS BABEŞ-BOLYAI
Engineering 70(1) 2025 DOI: 10.24193/subbeng.2025.1

Comparative Evaluation of Frequency-Based Indicators for Crack Detection

Ioana Ţincu, Gilbert-Rainer Gillich*, Vasile Cătălin Rusu

Abstract. *This paper compares three frequency-based damage indicators: the absolute frequency, the frequency difference, and the relative frequency shift (RFS). The indicators, calculated using mathematical relations developed by the authors, are used to create a database, and an artificial neural network (ANN) is trained on them. This network is used to assess cracks at various locations and with different depths. The frequencies obtained for these cracks are from ANSYS simulations. A comparison of the indicators is made to identify the most sensitive one. It was found that both the relative frequency shift and the frequency difference provide reliable and accurate crack position detection.*

Keywords*: Crack, Natural Frequency, Artificial Neural Network, Simulated Data, Sensitivity.*

1. Introduction

Frequency-based indicators are widely used in vibration-based structural health monitoring (SHM) because they are easy to acquire, robust to noise, and the acquisition equipment is simple and adequate for real-world measurements [1-3]. Still, their ability to detect early-stage cracks depends on how the frequency data is analyzed and compared. Small cracks can cause slight, mode-specific frequency changes that may be hidden by operational or environmental factors, such as shifts in boundary conditions, added mass, or temperature changes [4,5].

Cracks lower the local stiffness of beams and plates, making them more flexible and usually causing the natural frequencies of the affected modes to drop [6,7]. Therefore, the core of vibration-based crack detection is the link between local damage and frequency changes. There are several indicators based on changes in frequency due to damage and derived features, but neither a clear description of these indicators nor a systematic analysis of their effectiveness is provided in the literature.

Using absolute frequency alone is intuitive, but it can be affected by other factors that cause shifts similar to those caused by early damage [1,4]. The frequency difference, which is the deviation of the frequencies measured on a damaged beam from the baseline (i.e., the frequencies of the healthy beam), removes fixed offsets and is easy to interpret but is still sensitive to operational and environmental variability, such as changes in boundary conditions, mass loads, and temperature [2,5]. The relative frequency shift, defined as the normalized frequency difference relative to the baseline frequency, improves cross-mode comparability and ensures a good depiction of crack parameters [8].

This paper comparatively evaluates absolute frequency, frequency difference, and relative frequency shift arising from small to moderate cracks, quantifies performance in crack assessment using sensitivity indices, and discusses mode selection. The goal is to determine which indicator is most suitable for robust crack detection.

2. Typical Damage Indicators

For crack assessment, three closely related indicators are most common: absolute frequency, frequency difference, and relative frequency shift. Below, each indicator is defined, followed by practical strengths, limitations, and usage guidance in the presence of environmental and operational variability and mode-tracking issues.

The absolute frequency f_{iD} is defined as the measured natural frequency of the weak-axis bending vibration mode i in the current state. It is always lower than the baseline frequency f_i, which is the frequency of the healthy beam.

The frequency difference Δf_i is defined as the deviation from a healthy baseline. It is obtained by subtracting from the baseline f_i the frequency f_{iD} acquired after damage events; it highlights the changes accumulated after damage.

$$\Delta f_i = f_i - f_{iD} \tag{1}$$

Besides measurements, the frequency difference can be calculated if the location x and the crack depth a are known [9]. The authors derived the following mathematical relation:

$$\Delta f_i(x,a) = f_i - f_{iD}(x,a) = f_i \gamma(a)[\overline{\phi''}(x)]^2 \tag{2}$$

where $\gamma(a)$ is the damage severity and $\overline{\phi''}(x)$ is the normalized modal curvature. The curvature has a well-known relation for beams with different boundary conditions, while the severity can be calculated using the relation presented in [10] or by applying a fracture mechanics procedure [11].

The relative frequency shift $\Delta\overline{f_i}$ is defined as the normalized change relative to the baseline. Normalization promotes scale invariance, improving cross-mode comparability. The expression of the relative frequency shift is:

$$\Delta\overline{f_i} = \frac{f_i - f_{iD}}{f_i} \tag{3}$$

Besides measurements, the relative frequency shift can be calculated, for known damage location and depth, using the mathematical relation:

$$\Delta\overline{f_i}(x,a) = \frac{f_i - f_{iD}(x,a)}{f_i} = \gamma(a)[\overline{\phi''}(x)]^2 \tag{4}$$

An example of calculated data a specific input data (x and a) is presented in Table 1. In total, we generated 10,020 scenarios, including 501 locations and 20 severities. The complete dataset used in this study is publicly available in the project repository in [13]. This data is used to train the ANNs for the three indicator types.

Table 1. Example of damage indicators used to train the ANN.

Mode No.	f_i **[Hz]**	f_{iD} **[Hz]**	$\Delta f_i(x,a)$ **[Hz]**	$\Delta\overline{f}_i(x,a)$ **[Hz]**	x **[mm]**	a **[mm]**
1	4.0434	4.03685	$6.56781\cdot10^{-3}$	$1.62432\cdot10^{-3}$	288	1.045
2	25.3397	25.33116	$8.50084\cdot10^{-3}$	$3.35476\cdot10^{-4}$		
3	70.9518	70.81964	$1.32141\cdot10^{-1}$	$1.86240\cdot10^{-3}$		
4	139.0372	138.90376	$1.33415\cdot10^{-1}$	$9.59564\cdot10^{-4}$		
5	229.8384	229.82609	$1.23516\cdot10^{-2}$	$5.37406\cdot10^{-5}$		
6	343.3388	342.76311	$5.75720\cdot10^{-1}$	$1.67683\cdot10^{-3}$		

3. The ANN architecture and training process

3.1. Dataset Preprocessing

For each damage indicator (absolute frequency, frequency difference, and relative frequency shift), the generated database was combined into a single dataset containing all crack locations and severities. Since the objective of the ANN model is to predict only the crack position, the target variable was defined as the spatial coordinate x, while the selected modal quantities served as input features.

To ensure numerical stability and comparable scaling across modes, all input features were standardized using z-score normalization. For each feature z_i, normalization was performed as:

$$z_i^* = \frac{z_i - \mu_i}{\sigma_i} \tag{5}$$

where μ_i and σ_i denote the mean and standard deviation computed exclusively from the training subset. The same normalization parameters were subsequently applied to the validation and test subsets to prevent data leakage.

The dataset was randomly divided into training (70%), validation (15%), and test (15%) subsets. The training set was used for model parameter optimization, the validation set for hyperparameter tuning and early stopping, and the test set exclusively for final performance evaluation.

This preprocessing procedure was applied independently for each indicator type to ensure a fair comparison while maintaining consistent data handling.

3.2. Feature Analysis

Prior to defining the ANN architecture, a feature relevance analysis was conducted to identify the most informative vibration modes for crack localization. Although six bending modes were available for each damage indicator, not all contribute equally to predicting crack position. Since the implemented multilayer perceptron (MLP) model estimates only the crack location (and not the crack severity), the objective of this analysis was to determine which modal features provide the strongest and most robust spatial information.

For each indicator, the first six vibration modes were initially evaluated. Feature relevance was assessed using complementary metrics designed to capture different aspects of dependency between each modal quantity and crack position.

Pearson correlation was used to quantify linear association between each modal feature and crack position, indicating the strength and direction of a global linear relationship. Spearman correlation was computed to assess monotonic dependence, capturing nonlinear but consistently increasing or decreasing trends that Pearson correlation may not detect.

To identify more general nonlinear relationships, mutual information was calculated. This metric measures the reduction in uncertainty of crack position when a specific modal feature is known, regardless of whether the relationship is linear or monotonic.

Predictive relevance was further evaluated using permutation importance derived from a nonlinear ensemble model. This metric quantifies the decrease in prediction accuracy when the values of a given feature are randomly permuted, thereby reflecting how strongly the model relies on that feature.

Finally, the standalone predictive capability of each mode was assessed using cross-validated R^2 values obtained from single-feature regression models. The R^2 metric represents the proportion of variance in crack position explained by one modal feature alone and serves as a direct indicator of identifiability.

These metrics were selected to ensure that feature selection was not biased toward a single modeling assumption, combining linear, monotonic, nonlinear, and predictive perspectives. All analyses were performed exclusively on the training subset to avoid data leakage.

The results consistently showed that the lower-order modes dominate crack localization performance for all three indicators. Mode 1 exhibited the strongest association and predictive power, followed by Modes 2 and 3. Mode 4 provided additional but smaller contributions, while Modes 5 and 6 showed limited standalone relevance and marginal incremental benefit. This behavior is consistent with beam theory, as lower bending modes are more sensitive to global stiffness reductions caused by cracks.

Based on this analysis, the four most significant modes (Modes 1-4) were selected as input features for the ANN model for each damage indicator. This reduced feature set preserves the dominant spatial information while limiting model complexity and reducing the risk of overfitting. The subsequent section presents the ANN architecture and training procedure used for crack position prediction.

3.3. ANN Architecture and Training Procedure

A multilayer perceptron (MLP) architecture was adopted for crack position prediction [14]. The network consisted of an input layer corresponding to the selected modal features (Modes 1-4), a single hidden layer with a fixed number of neurons, and one output neuron representing the predicted crack position $\hat{\boldsymbol{x}}$.

The hidden layer employed the Rectified Linear Unit (ReLU) activation function:

$$ReLU(u) = \max(0, u) \tag{6}$$

The output layer was linear, as crack position prediction represents a regression problem.

Model parameters were optimized using the AdamW optimizer with L2 regularization (weight decay) to reduce overfitting. The training objective was to minimize the Mean Squared Error (MSE):

$$MSE = \frac{1}{N}\sum_{j=1}^{N}\left(x_j - \hat{x}_j\right)^2 \tag{7}$$

where x_j is the true crack position and $\hat{x}_j$ is the predicted position.

Training was performed for a predefined maximum number of epochs. Early stopping was implemented based on validation RMSE; training was terminated if validation performance did not improve for a specified number of consecutive epochs. To ensure reproducibility and a fair comparison between indicators, the network architecture and training hyperparameters were kept identical across all experiments.

3.4. Evaluation Metrics and Results

Model performance was evaluated using three standard regression metrics [15]. A brief description of the metrics is given below.

Mean Absolute Error (MAE) represents the average absolute deviation between predicted and true crack positions and has a direct physical interpretation in units of beam length.

$$MAE = \frac{1}{N}\sum_{j=1}^{N}\left|x_j - \hat{x}_j\right| \tag{8}$$

Root Mean Squared Error (RMSE) penalizes larger errors more strongly than MAE and provides an overall measure of prediction accuracy.

$$RMSE = \sqrt{\frac{1}{N}\sum_{j=1}^{N}\left(x_j - \hat{x}_j\right)^2} \tag{9}$$

Coefficient of Determination (R^2) quantifies the proportion of variance in crack position explained by the model. $\bar{x}$ is the mean crack position in the dataset

$$R^2 = 1 - \frac{\sum_{j=1}^{N}\left(x_j - \hat{x}_j\right)^2}{\sum_{j=1}^{N}\left(x_j - \bar{x}\right)^2} \tag{10}$$

3.5. Training Results and Interpretation

The comparative training results indicate that all three indicators enable accurate crack position prediction under simulated conditions. Among them, models trained using absolute frequencies achieved the lowest RMSE and the highest R^2 values. The relative frequency shift and frequency difference exhibited nearly identical performance, with slightly higher prediction errors but still strong explanatory capability. These findings suggest that, within a controlled simulation framework where environmental and operational variability are absent, all three frequency-based indicators contain sufficient spatial information for reliable crack localization.

The slight performance differences observed among indicators reflect variations in their sensitivity characteristics but do not significantly affect predictive capability in the considered scenario.

4. Sensitivity Analysis

To further evaluate the robustness of the trained ANN models, a sensitivity analysis was conducted using new frequency measurements obtained from finite element simulations. Unlike the datasets used for training, these scenarios were not included in the learning process and therefore represent an independent validation of the predictive capability of each damage indicator.

The analyzed scenarios correspond to a fixed crack depth of $a = 1\ mm$ while the crack location was varied along the beam length. For each scenario, the first four natural frequencies of the damaged beam f_{iD} (Modes 1-4) were extracted from the modal analysis module performed using ANSYS. These frequencies were used to compute the associated damage indicators. The previously trained ANN models were then used to predict the crack position. The results are summarized in Table 2.

Table 2. Numerical simulation data used to assess the indicators' sensitivity.

f_{1D} [Hz]	f_{2D} [Hz]	f_{3D} [Hz]	f_{4D} [Hz]	x [mm]	$\hat{x}$ with f_{iD} [mm]	$\hat{x}$ with $\Delta f_i(x,a)$ [mm]	$\hat{x}$ with $\Delta \bar{f}_i(x,a)$ [mm]
4.0452	25.4108	71.2916	139.9644	34	34476.63	37.33	37.12
4.07181	25.6031	71.3911	140.2604	288	202382.05	300.79	300.07
4.07553	25.5679	71.4045	140.5964	338	208919.74	343.85	344.69
4.08367	25.4733	71.7518	139.8021	486	245474.33	490.52	490.34
4.08468	25.4680	71.7482	139.7996	512	248596.15	501.65	501.49
4.08518	25.4670	71.7316	139.8536	526	249491.18	535.06	535.38
4.08570	25.4675	71.7009	139.9555	542	249887.60	548.35	548.52
4.08921	25.5570	71.2662	140.0709	724	265808.90	739.27	740.10
4.08963	25.5932	71.4019	139.6646	788	283383.30	762.77	763.35
4.08979	25.6123	71.5634	139.8527	838	295376.83	831.06	831.11
4.08988	25.6260	71.7461	140.5731	938	303909.18	913.72	913.59

The natural frequencies for the intact beam are:
$f_1 = 4.0899$ Hz, $f_2 = 25.6265$ Hz, $f_3 = 71.7547$ Hz, $f_4 = 140.6276$ Hz.

Table 3. ANN performance metrics for FEM scenarios.

Damage Indicator	MAE	RMSE	R^2
f_{iD}	234.699263	244.936230	-934330.128734
$\Delta f_i(x,a)$	0.011270	0.013370	0.997216
$\Delta \overline{f_i}(x,a)$	0.011336	0.013384	0.997210

5. Discussion

The results clearly indicate a fundamental difference in robustness among the considered indicators when applied to new frequency measurements.

The models trained using the relative frequency shift and the frequency difference maintain excellent predictive accuracy, with very small absolute errors and near-perfect R^2 values. The predicted crack locations closely follow the true spatial positions along the entire beam length.

In contrast, the model trained using absolute damaged frequencies fails under the same conditions. The predicted crack positions become physically unrealistic, leading to extremely large errors and a strongly negative R^2. This behavior indicates that absolute frequency is highly sensitive to variations between the training dataset and the new measurement scenarios.

The underlying reason lies in the scale dependence of absolute frequency. While absolute frequencies performed well within the controlled training dataset, they are strongly influenced by global system properties such as stiffness scaling, modeling assumptions, or boundary condition variations. In contrast, both the frequency difference Δf_i and the relative frequency shift normalize the frequency variation with respect to the healthy baseline, thereby reducing sensitivity to global offsets and improving cross-scenario generalization.

6. Conclusion

This study comparatively evaluates three frequency-based damage indicators, namely the absolute frequency, the frequency difference, and the relative frequency shift, for ANN-based crack position detection in beams. A feature relevance analysis

demonstrated that the lower bending modes contain the most significant spatial information, and the first four modes were selected as inputs to a baseline multilayer perceptron model.

Under controlled simulation conditions, all indicators enabled accurate crack localization. However, when applied to new frequency measurements obtained from finite element simulations, clear differences in robustness were observed. The relative frequency shift and the frequency difference maintained excellent predictive capability, whereas the model trained on absolute frequencies exhibited large errors and poor generalization.

The baseline MLP predicted the crack position with an average error of approximately 1 cm when using either the relative frequency shifts or the frequency differences as input features. These results confirm that normalized frequency-based indicators provide superior robustness and reliability for crack localization.

As future work, the influence of neural network topology should be further investigated to reduce the prediction error. In particular, alternative architectures and connectivity structures may improve the representation of nonlinear relationships and enhance generalization performance.

References

1 Salawu O.S., Detection of structural damage through changes in frequency: A review, *Engineering Structures*, 19(9), 1997, pp. 718–723.

2 Doebling S.W., Farrar C.R., Prime M.B., A summary review of vibration-based damage identification methods, *Shock and Vibration Digest*, 30(2), 1998, pp. 91–105.

3 Farrar C.R., Worden K., Structural Health Monitoring: A Machine Learning Perspective, *Wiley*, 2012.
(Example for Internet sources)

4 Peeters B., De Roeck G., One-year monitoring of the Z24-Bridge: Environmental effects versus damage events, *Earthquake Engineering & Structural Dynamics*, 30(2), 2001, pp. 149–171.

5 Deraemaeker A., Reynders E., De Roeck G., Kullaa J., Vibration-based structural health monitoring using output-only measurements under changing environment, *Mechanical Systems and Signal Processing*, 22(1), 2008, pp. 34–56.

6 Dimarogonas A.D., Vibration of cracked structures: A state of the art review, *Engineering Fracture Mechanics*, 55(5), 1996, pp. 831–857.

7 Cawley P., Adams R.D., The location of defects in structures from measurements of natural frequencies, *Journal of Strain Analysis for Engineering Design*, 14(2), 1979, pp. 49–57.

8 Gillich G.R., Maia N.M.M., Wahab M.A., Tufisi C., Korka Z.I., Gillich N., Pop M.V., Damage detection on a beam with multiple cracks: A simplified method based on relative frequency shifts, *Sensors*, 21(15), 2021, paper ID 5215.
9 Gillich G.R., Tufoi M., Korka Z.I., Stanciu E., Petrica A., The Relations between Deflection, Stored Energy and Natural Frequencies, with Application in Damage Detection, *Romanian Journal of Acoustics and Vibration*, 13(2), 2016, pp. 87–93.
10 Gillich G.R., Maia N., Mituletu I.C., Tufoi M., Iancu V., Korka Z., A new approach for severity estimation of transversal cracks in multi-layered beams, *Latin American Journal of Solids and Structures*, 13 (8), 2016, pp. 1526–1544.
11 Ostachowicz W.M., Krawczuk C., Analysis of the effect of cracks on the natural frequencies of a cantilever beam, *Journal of Sound and Vibration*, 150(2), 1991, pp. 191–201.
12 Praisach Z.I., Minda F.P., Gillich G.R., Minda A.A., Relative frequency shift curves fitting using FEM modal analyses, *Proceedings of the 4th WSEAS international conference on Finite Differences – Finite Elements – Finite Volumes – Boundary Elements*, 2021, pp. 82–87.
13 https://github.com/IoanaTincu/Studia-Universitatis-Babes-Bolyai-Engineering
14 Goodfellow I., Bengio Y., Courville A., Deep Learning, MIT Press, Cambridge, MA, 2016.
15 Haykin S., Neural Networks and Learning Machines, 3rd ed., Pearson Education, Upper Saddle River, NJ, 2009.

Addresses:

- Ph.D. Stud. Ioana Ţincu, Babeș-Bolyai University, Doctoral School of Engineering, P-ta Traian Vuia 1–4, 320085 Reșița, Romania
ioana.tincu@ubbcluj.ro
- Prof. Gilbert-Rainer Gillich, Babeș-Bolyai University, Doctoral School of Engineering, P-ta Traian Vuia 1–4, 320085 Reșița, Romania
https://orcid.org/0000-0003-4962-2567
gilbert.gillich@ubbcluj.ro
(**corresponding author*)
- Dr. Vasile-Cătălin Rusu, Babeș-Bolyai University, Department of Computer Science, Str. Mihail Kogălniceanu nr. 1, RO-400084 Cluj-Napoca, Romania
vasile.rusu@ubbcluj.ro

STUDIA UNIVERSITATIS BABEŞ-BOLYAI
Engineering 70(1) 2025 DOI: 10.24193/subbeng.2025.2

Advanced Modal Analysis Technique for Structures with Non-Uniform Mass Distribution

Rusalin Lucian Paun, Gilbert-Rainer Gillich*, Mitsinjo Randrianarisoa

Abstract. *This paper presents a study of how the natural frequencies of bending vibration modes change for a double-clamped beam with a concentrated mass added to the beam mid-span. We compare the beam's response under different loads using a contrived analytical relation and experimental results. The results show that we can estimate a small variation in mass distribution and that the frequency estimation method, especially developed by the authors to capture slight structural, is effective.*

Keywords*: Non-uniform mass distribution, Frequency estimation technique, Modal analysis, Analytical method, Experiment.*

1. Introduction

It is often necessary to know the natural frequencies of mechanical systems [1]-[3] and how they change when the structure changes, for example, by adding mass [4],[5]. There are several ways to find these frequency changes [6]. Impulsive force-based excitation techniques are simple and low-cost; they also produce broadband excitation, but the amplitudes of the higher-order natural frequencies decay quickly [7]. The signal-to-noise ratio (SNR) is low, and repeatability is poor, limiting the method's accuracy. The use of non-impact excitation techniques is often preferred to impact methods [8,9], especially in laboratory conditions. However, this procedure is more complicated and time-consuming.

Methods using sinusoidal excitation easily ensure test repeatability due to the stability of the excitation signal parameters [10]. Each frequency of interest can be analyzed separately; simulations can also be performed around each frequency of interest or in a broadband manner, modifying the excitation signal in various ways [11], thereby reducing the analysis time. The analysis time can also be reduced by using appropriate response analysis methods [12].

If physical contact with the tested structure is not allowed, not efficient, or impossible, non-contact excitation techniques are applied, for example, acoustical excitation. The method is suitable for lightweight structures and allows control of various parameters of the energy transferred to the structure [13]. This controlled energy transfer reduces the effects of noise, especially when the vibration modes are analyzed separately.

The addition of mass modifies the structure's natural frequencies, with changes that depend on the mode number and the position of the added mass. In this paper, we evaluate the sensitivity of the proposed modal analysis technique to added mass.

2. Frequency Changes due to Added Mass

In this paper, we perform experiments on a prismatic fiberglass beam fixed at both ends. The specimen has the following dimensions: length L = 0.78 m, thickness H = 0.003 m, and width B = 0.02 m. For these data, the cross-sectional area is $A = 60 \cdot 10^{-6}$ m^2 and the second moment of inertia is $I = 4.5 \cdot 10^{-11}$ m^4. The Young modulus provided by the producer for the fiberglass is $E = 2.6 \cdot 10^{10}$ N/m^2, and the mass density is ρ = 1800 kg/m^3. This mass density value was confirmed by experiments conducted as part of this research.

The research focuses on testing the sensitivity of a developed experimental modal analysis technique to slight changes in a structure's mass. To this end, we consider in the study the weight of the accelerometer m_a = 8 g, and three supplementary masses, m_1 = 0.5 g, m_2 = 1 g, and m_3 = 2.33 g.

For the beam without supplementary mass, we calculate the first five natural frequencies of the fiberglass beam with the formula:

$$f_i = \frac{\lambda^2}{2\pi L^2}\sqrt{\frac{EI}{\rho AL}} \tag{1}$$

In Eq. (1), we denote with λ the eigenvalues for the double-clamped beam. The first five weak-axis bending vibration modes of the beam are given in Table 1.

To calculate the frequencies of the beam with an added mass, f_{iR}, we used mathematical relation deduced by the authors [14].

$$f_{Ri} = f_i \sqrt{\frac{\lambda_i^{0-L}}{\lambda_i^{0-a} + \lambda_i^{a-b}\frac{\bar{m}_R}{\bar{m}} + \lambda_i^{b-L}}} \tag{2}$$

where

$$\lambda_i^{0-a} = \int_0^a \left[\bar{f}_i(x)\right]^2 dx, \quad \lambda_i^{a-b} = \int_a^b \left[\bar{f}_i(x)\right]^2 dx, \ldots \lambda_i^{b-L} = \int_b^L \left[\bar{f}_i(x)\right]^2 dx \tag{3}$$

are mass participation coefficients, and represent the square of the normalized mode shapes on segments 0-*a*, *a*-*b*, and *b*-*L*. With $\bar{m}$ we denoted the distributed mass of the beam, and with $\bar{m}_R$ the distributed mass of the segment where the supplementary loads act.

The analyzed beam is shown on Fig. 1. It has both ends fixed and on the mid-span, on a segment of 10 mm length, is applied the supplementary mass. On one face it is mounted an accelerometer, on the other the masses. The frequency of the beam is calculated with the mounted accelerometer and afterward adding different weights. The results are presented in Table 1. One can observe that the frequency drops significantly due to the accelerometer.

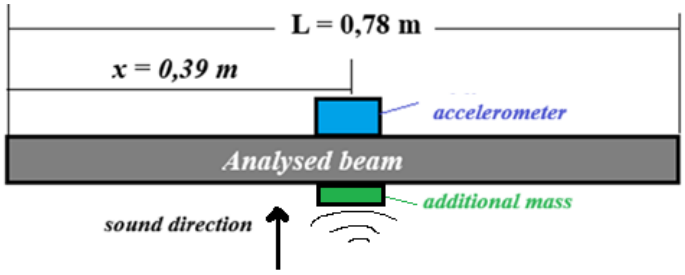

Figure 1. The text of figure caption. (TNR, 11, Normal)

Table 1. The calculated frequencies for the first five bending vibration modes.

Frequency / Mass	f_1 [Hz]	f_2 [Hz]	f_3 [Hz]	f_4 [Hz]	f_5 [Hz]
No mass	19.26	53.1	104.1	172.1	257.1
m_a = 8 g	17.24	53.09	92.10	172.05	235.14
$m_a + m_1$ = 8.5 g	17.14	53.09	91.20	172.04	233.95
$m_a + m_2$ = 9 g	17.03	53.09	90.90	172.04	232.78
$m_a + m_3$ = 10.33 g	16.77	53.09	89.90	172.03	229.74
$m_a+m_1+m_2+m_3$ = 11.83 g	16.48	53.09	88.25	172.02	226.45

3. Experimental validation

In this section we will focus on vibration mode three. The experimental setup is presented in Figure 2 and 3. The excitation is realized with a sinusoidal sound wave signal of constant amplitude, with a frequency near the calculated frequencies for the beam with the accelerometer and additional masses placed in the middle. The signal is 0.1 Vpp. The excitation signal is generated by a signal generator, amplified, and transmitted to the speaker. Acoustic vibrations are induced in the beam using a low-frequency speaker with an impedance of 4 ohms and a power of 50 watts. The speaker is positioned directly in front of the beam, centered on its midpoint, approximately 0.04...0.05 m away, to minimize vibration energy losses. The speaker's position can be adjusted. Measurement is realized in LabVIEW using a Kistler 8772A5 one-axis accelerometer, connected to the four-channel NI cDAQ-9172 module. The received signal is converted and sent to a laptop, where it is stored, processed, and displayed.

Figure 2. The experimental stand – control and measurement system

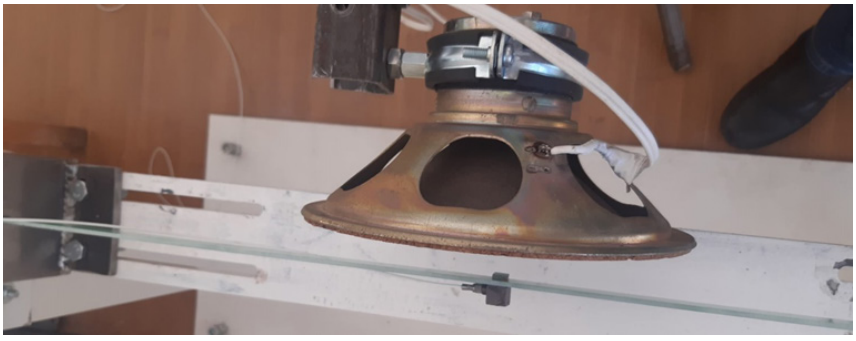

Figure 3. The beam with accelerometer and weight and the excitation system (upper view)

To accurately find the natural frequencies, a technique presented in [13] is used. It presumes exciting the structure with frequencies around the presumed natural frequency and targeting a response that does not mimic the beetle phenomenon. Figure 4 shows a vibration signal acquired for an excitation frequency that does not match the natural frequency of the beam. One can observe that the amplitude increase and decrease, which means the resonance frequency is not achieved.

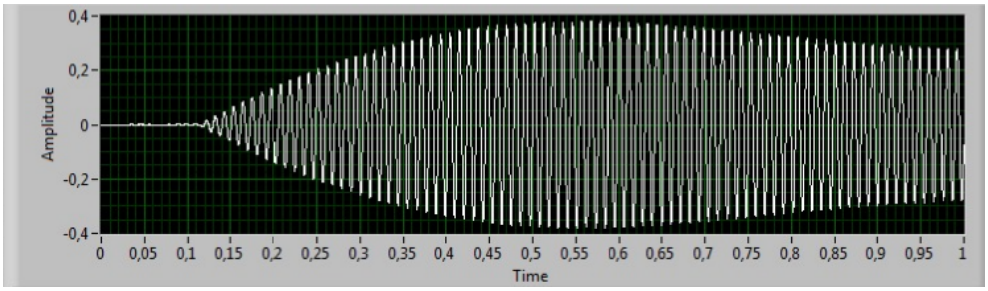

Figure 4. Beam response to an excitation with the frequency that does not fit the resonance frequency

In contrast, Figure 5 shows a response acquired when the excitation and natural frequency fit. One can observe that the amplitude increases constantly and is significantly higher than that in Figure 4.

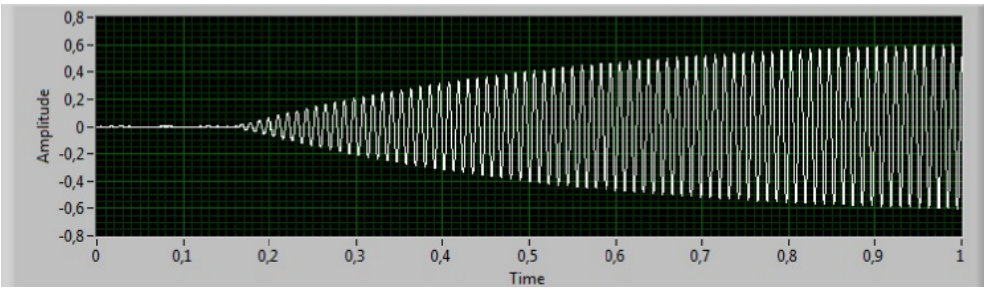

Figure 5. Beam response to an excitation with the frequency that fits the resonance frequency

The spectrum of the vibration signal depicted above is plotted in Figure 6. With blue color we represent the spectrum on a larger range around the natural frequency domain, and a zoom on the peak is shown with a red color in the small window. One can observe that the neighbors of the maximizer have equal amplitudes, which means the frequency is correctly estimated.

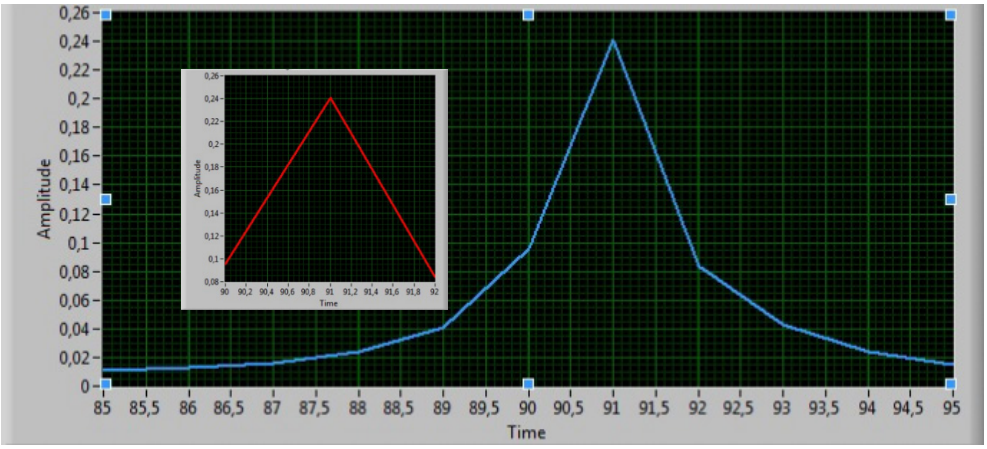

Figure 6. Detail on the frequency spectrum and a zoom on the peak frequency

The frequency estimates made for the signals acquired when the beam was excited with the correct frequencies are presented in Table 2.

Table 2. The estimated frequencies for the first five bending vibration modes.

Frequency / **Mass**	f_1 **[Hz]**	f_2 **[Hz]**	f_3 **[Hz]**	f_4 **[Hz]**	f_5 **[Hz]**
No mass	-	-	-	-	-
m_a = 8 g	17.24	53.09	92.10	172.05	235.14
$m_a + m_1$ = 8.5 g	17.14	53.09	91.20	172.04	233.95
$m_a + m_2$ = 9 g	17.03	53.09	90.90	172.04	232.78
$m_a + m_3$ = 10.33 g	16.77	53.09	89.90	172.03	229.74
$m_a+m_1+m_2+m_3$ = 11.83 g	16.48	53.09	88.25	172.02	226.45

To test if small frequency changes can be identified using the advanced technique proposed by the authors, we represent the calculated frequencies and those obtained from measurements. One can observe that the frequency evolution with the mass increase is similar, which demonstrates the mathematical relation (2) is correct and the frequency estimation technique is reliable and allows obtaining accurate estimations.

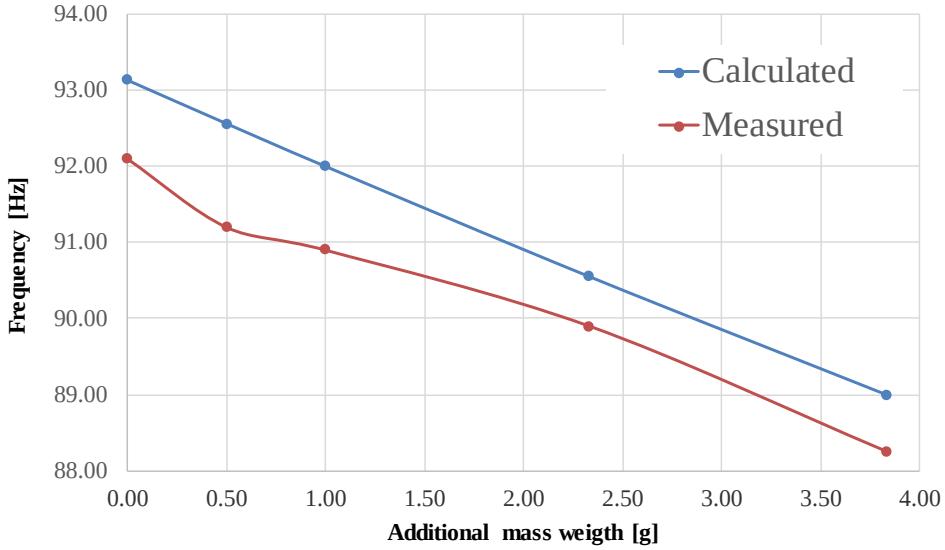

Figure 7. Comparison of calculated and measured frequencies

It can be also observed in Figure 7 that, for small mass changes, the error is bigger. However, the difference is small and because it is approximately the same for all additional weights, it is provoked by the mechanical and physical characteristics used in calculus.

4. Conclusion

This study investigated several key aspects of experimental modal analysis performed on a double-clamped fiberglass beam, with a particular focus on the influence of added mass and the precision required for accurate frequency estimation. The work provides both methodological insights and practical considerations relevant to lightweight structures, where even minimal mass perturbations can significantly affect dynamic properties.

A central contribution of the research is the mathematical relation derived by the authors, which quantifies the effect of the accelerometer's added mass on the measured natural frequencies. The results demonstrate that, for lightweight structures such as the fiberglass beam examined here, this corrective relation is not merely useful but mandatory for obtaining the true, unaltered natural frequencies. By compensating for mass-loading effects, the method ensures that the modal parameters reflect the actual behavior of the structure rather than artifacts introduced by the measurement system.

Another significant finding is the high sensitivity of the proposed frequency estimation technique. The method successfully identifies frequency shifts on the order of hundredths, highlighting its suitability for applications requiring elevated precision, such as early-stage damage detection, structural health monitoring, and quality control in manufacturing processes. Such fine resolution is essential when working with structures where small changes in stiffness, mass, or boundary conditions must be detected reliably.

Moreover, the study shows that slight variations in mass are not only observable but can be quantified directly through the resulting frequency changes. The experimental setup enabled the clear detection of a 0.5-gram increase in mass, underscoring the technique's capability to capture minute alterations in structural properties. This level of sensitivity strengthens the method's relevance for monitoring lightweight composite components or any system where minimal mass fluctuations may signify degradation or external influence.

Overall, the findings confirm that accurate modal characterization of lightweight structures requires careful consideration of measurement influences, refined signal-processing techniques, and high-resolution frequency estimation. The methods developed and validated in this study provide a robust foundation for further advancements in non-destructive evaluation and precision modal analysis.

References

1 Tianlong Z., Dapeng S., Zhuo W., Peng Z., Shiming W., Xiaoyu D., *Vibration-based structural damage detection via phase-based motion estimation using convolutional neural networks*, Mechanical Systems and Signal Processing, 178, 2022, Art. ID 109320.

2 Radeș M., *Vibrații mecanice*, Editura Printech, 2008

3 Bratu P., *Vibrațiile sistemelor elastice*, Editura Tehnică, București, 2000.

4 Praisach Z., Gillich G.R., Birdeanu D.E., *Considerations on natural frequency changes in damaged cantilever beams using FEM*, International Conference on Engineering Mechanics, Structures, Engineering Geology, International Conference on Geography and Geology - Proceedings, 2010, pp. 214-219.

5 Gillich G.R., Praisach Z.I., *Damage-patterns based method to locate discontinuities in beams*, Proceedings of SPIE - The International Society for Optical Engineering, 8695, 2013.

6 Silva J.M.M., Maia N.M.M., Modal Analysis and Testing, *NATO Science Series E* 363, Springer, 1999.

7 Gillich, G.R., Minda, P.F., Praisach, Z.-I., Minda, A.A., Natural frequencies of damaged beams - a new approach, *Romanian Journal of Acoustics and Vibration*, 9(2), 2012, pp. 101-108.

8 Brown D.L., R.J. Allemang, A.W. Phillips, Forty years of use and abuse of impact testing: a practical guide to making good FRF measurements, in: J. De Clerck (Ed.), Experimental Techniques, Rotating Machinery, and Acoustics, 8, 2015, pp. 221–241.
9 Wei Y., Dong Y., Huang X., Zhang Z., A stepped frequency sweeping method for nonlinearity measurement of microresonators, *Sensors*, 16(10), 2016, Art ID 1700.
10 Van der Auweraer H., Vanherck P., Sas P., Snoeys R., Accurate modal analysis measurements with programmed sine wave excitation, *Mechanical Systems and Signal Processing*, 1(3), 1987, pp. 301–313.
11 Friswell M.I., Penny J.E.T., Stepped sine testing using recursive estimation, Mechanical Systems and Signal Processing, 7(6), 1993, pp. 477–491.
12 Maia N.M.M., Silva J.M.M., Modal analysis identification techniques, *Philos. Trans. R. Soc. A*, 359(1778), 2001, pp. 29–40.
13 Hamat C.O., Paun RL., Gillich, GR., Iterative Frequency Excitation Technique for Accurate Modal Analysis, Acoustics and Vibration of Mechanical Structures—AVMS-2025, *Springer Proceedings in Physics*, 345, 2025, pp. 320-330.
14 Gillich G.R., Praisach Z.I., Iancu V., Furdui H., Negru I., Natural Frequency Changes due to Severe Corrosion in Metallic Structures, *Strojniški vestnik - Journal of Mechanical Engineering*, 61(12), 2015, pp. 721-730.

Addresses:

- Ph.D. Stud. Rusalin Lucian Paun, Babeș-Bolyai University, Doctoral School of Engineering, P-ta Traian Vuia 1–4, 320085 Reșița, Romania
rusalin.paun@ubbcluj.ro
- Prof. Gilbert-Rainer Gillich, Babeș-Bolyai University, Doctoral School of Engineering, P-ta Traian Vuia 1–4, 320085 Reșița, Romania
gilbert.gillich@ubbcluj.ro
(*corresponding author)
- Assoc. prof. Mitsinjo Randrianarisoa, Institut Supérieur de Technologie d'Antananarivo, Antananarivo 101, Madagascar
ramitsinjo@yahoo.fr

STUDIA UNIVERSITATIS BABEŞ-BOLYAI
Engineering 70(1) 2025 DOI: 10.24193/subbeng.2025.3

Influence of Infill Density on Dimensional and Geometrical Deviations of PLA Parts Fabricated by FDM

Raul-Rusalin Turiac, Zoltan-Iosif Korka*, Alexandra-Teodora Aman, Mihael Magda

Abstract. *The study investigates the influence of infill density on the dimensional and geometric deviations of Polylactic Acid (PLA) cubic specimens manufactured using Fused Deposition Modeling (FDM). Five infill levels (20–100%) were analyzed, while all other process parameters were kept constant. Flatness, parallelism, perpendicularity, and dimensional measurements were performed using a Mitutoyo MiSTAR 555 coordinate measuring machine, providing micron-level accuracy. The results show that infill density has selective and direction-dependent effects on geometric accuracy, without indicating a general trend applicable to all types of deviations. A linear increase in printing time and specimen mass was also observed as infill density increased, indicating a direct impact on manufacturing cost.*

Keywords*: Fused Deposition Modeling (FDM), Polylactic Acid (PLA), Infill Density, Dimensional Accuracy, Geometrical Deviations*

1. Introduction

Three-dimensional printing using Fused Deposition Modeling (FDM) has advanced significantly in recent years, becoming one of the most widely used methods for the rapid fabrication of prototypes and functional polymer components. The technology operates by the controlled extrusion of a heated thermoplastic filament, which is deposited layer by layer according to a previously generated digital model. The simplicity of the process, the relatively low equipment cost, and the ability to produce complex geometries have contributed decisively to its widespread adoption in industrial, educational, and research environments.

However, the layer-by-layer nature of FDM parts introduces variability that can affect surface quality, dimensional accuracy, and the mechanical behavior of the final products. In practice, parts manufactured via FDM may exhibit deviations from their designed dimensions, phenomena often associated with the ways in which process parameters influence the deposition of the molten material. Parameters such as printing speed, filament color, layer thickness, or printing strategy [1-3] are only a few of the factors that determine the dimensional stability of components produced by this technology.

Although the literature addresses a wide range of process parameters, the density and pattern of the infill remain comparatively less explored than variables such as temperature, speed, or printing orientation. The infill represents the internal structure of the part and can be configured in various geometric patterns (rectilinear, concentric, honeycomb, HilbertCurve, and others), each distributing material differently throughout the volume and influencing both internal stiffness and the way the part stabilizes dimensionally.

In their study, Khan et al. [4] analyzed the tensile and flexural behavior of PLA specimens with different infill patterns and observed that the rectilinear structure generated the highest values of strength and elastic modulus (19.1 MPa and E = 10.51 GPa in tension; 24.4 MPa and E= 0.359 GPa in flexure), whereas the HilbertCurve pattern resulted in the lowest mechanical performance.

Infill density is another parameter that directly influences the mechanical behavior of FDM-manufactured parts due to its role in the internal distribution of material and in the way, loads are transmitted throughout the structure. Abdulridha et al. [5] highlight the essential importance of this parameter, showing that infill density exhibits the highest statistical significance on the compressive strength of PLA specimens, with values increasing from approximately 4 MPa to 56.5 MPa as the density is raised from 20% to 100%.

Similarly, various research studies conclude that denser internal structures reduce porosity, improve interlayer cohesion, and provide superior mechanical performance. The results reported in recent research consistently indicate that high infill density leads to increases in stiffness, tensile strength, and elastic modulus, regardless of the infill pattern used [6-10].

For applications, in which geometric accuracy is critical, understanding how infill density alters material distribution and the shrinkage or post-deposition stabilization processes, becomes essential. In the specialized literature, several studies confirm that infill influences the dimensional deviations of PLA parts. Alafaghani et al. [11] report that infill percentage is among the most influential parameters affecting dimensional accuracy: low values (20%) generate the smallest cumulative errors, whereas 100% infill leads to oversizing due to excessive material accumulation. Similarly, Abas et al. [12] report increases in deviations as density is raised from 20% to 50%, the deviation in length increases from ~0.4% to 0.9%, in width from ~1.1% to 2.0%, and in height from ~1.0% to 1.3%, with deformations confirmed microscopically. Comparable results are presented by Zonoobi et al. [13], where densities of 10%, 30%, and 50%

show that infill is the second most influential factor affecting dimensional errors (after layer thickness), with the smallest deviations obtained at 10% infill and the largest at 50%. Solouki et al. [14] confirm the same moderate trend: increasing infill from 60% to 80% leads to slight increases in deviations (length: 0.75–0.78 mm; width: 0.31–0.35 mm), depth deviation although decreases (0.015–0.01 mm).

However, certain studies identify the presence of optimal infill levels. Singh et al. [15] observe that dimensional accuracy is highest at 40% infill; higher values (60–80%) generate internal stresses and amplify deviations. Similarly, Galetto et al. [16], analyzing the 5–20% range, show that intermediate values (13–19%) provide the best dimensional accuracy, without revealing a global monotonic trend. Gunes et al. [17] confirm that the effect of infill density is not systematic, with variations depending on part geometry: each shape exhibits its own optimal density range for minimizing deviations. In a broader analysis covering 10–100%, Vălean et al. [18] report very small deviations (below 0.14%), with the lowest errors at 90% infill, while low-density levels (10–30%) show the highest variability. Miron et al. [18], analyzing densities between 20–100%, identify a maximum error of ~0.9% in specimen width, which tends to decrease as infill increases, whereas deviations in length and thickness do not follow a clear trend.

Overall, the literature shows that infill density can influence dimensional accuracy; however, the conclusions are inconsistent, primarily because most studies simultaneously modify multiple process parameters (layer height, orientation, speed, temperature, infill pattern), making it difficult to isolate the specific effect of infill density. Furthermore, some studies do not fully report experimental conditions, part geometry, or measurement methods, limiting the formulation of a universally valid relationship between infill and dimensional deviations.

In this context, the present study aims to directly investigate the influence of infill density on the dimensional deviations of PLA parts manufactured via FDM, varying exclusively this parameter throughout the experiment. The novelty of the study lies not only in isolating the effect of infill density but also in the depth of the analysis: dimensional deviations are evaluated using high-precision metrological equipment capable of detecting micron-level variations, allowing for a much more accurate characterization of geometric behavior. In addition, essential components of part performance (surface flatness, parallelism, and perpendicularity) are analyzed alongside the influence of infill density on printing time and material consumption, factors highly relevant for optimizing manufacturing costs.

2. Materials and Methods

To examine the influence of infill density on dimensional deviations, a batch of 25 cubic test samples (5 specimens for each infill density of 20, 40, 60, 80 and 100%) was manufactured using FDM technology. The geometry of the samples and their nominal dimensions are presented in Figure 1.

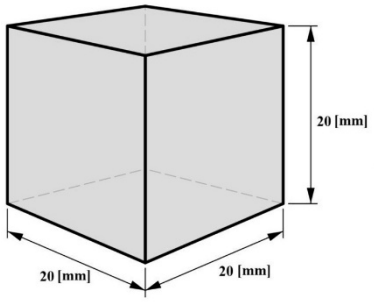

Figure 1. Geometry of the cubic test specimen and its nominal dimensions

2.1. Printing of the Test Specimens

The test specimens were printed on a Creality Ender-3 V3 KE printer using Polymaker PLA Panchroma filament in satin black. The process parameters were kept constant throughout the fabrication of the entire batch, with their values listed in Table 1. The only experimental variable was the infill density, for which five levels were selected. Five specimens were manufactured for each level to achieve the highest possible measurement accuracy.

Table 1. Process parameters used for printing the test specimens

Material	PLA
Filament diameter	1.75 mm
Nozzle diameter	0.4 mm
Extruder temperature	210 °C
Printing bed temperature	60 °C
Layer thickness	0.20 mm
Printing speed	50 mm/s
Fan	Yes, at 50% of the maximum power
Orientation	YX
Infill raster angle	0°/90°
Infill density	20 / 40 / 60 / 80 / 100 %
Infill pattern	Gyroid
Number of contour lines	2
Top layers	4
Bottom layers	4
Top/Bottom pattern	Zig Zag
Top/Bottom raster angle	45°/135°

In the case of the gyroid infill pattern, the internal structure is generated parametrically by the slicer as a triply periodic minimal surface (TPMS). Consequently, the raster angle parameter does not significantly alter the internal geometry in the same manner as in linear or grid infill patterns, where strand orientation directly governs structural anisotropy.

To illustrate the variation of the internal structure as a function of infill density, Figure 2 shows the slicer-generated renderings (Creality Print) for layer 50 of the specimens, selected as an intermediate level from the total of 100 layers that form the final geometry.

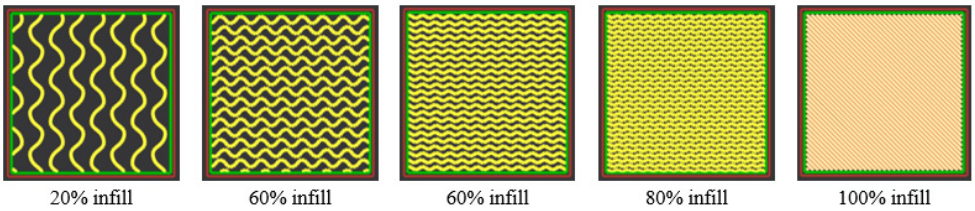

Figure 2. Internal structure at layer 50 for different infill densities

It should be noted that at 100% infill density, the slicing software generates a fully solid structure, and the selected infill pattern no longer governs the internal geometry. In this case, the internal region is filled using the same configuration as the solid top and bottom layers, namely a Zig Zag pattern with a raster angle of 45°/135°. This behavior results from the slicer's default solid-fill strategy rather than from a modification of the experimental parameters.

2.2. Dimensional Measurements

To identify the influence of infill density on the PLA specimens, both dimensional measurements along the three principal directions of the cubic samples and geometric form deviations were performed. These included the deviations from flatness for all cube faces, the parallelism deviations between opposite faces, and the perpendicularity deviation between all adjacent faces.

The measurements were carried out using a Mitutoyo MiSTAR 555 Coordinate Measuring Machine (CMM), equipped with a Renishaw SP25M scanning probe and SM25-1 module, fitted with a ruby-tipped stylus of size M3 fixture, length 31 mm and 4 mm ball diameter. Data acquisition and measurement processing were performed using the CAT1000 and GEOPAK software modules. The equipment used is illustrated in Figures 3(a) and 3(b).

a b

Figure 3. Mitutoyo MiSTAR 555 coordinate measuring machine and specimen setup for dimensional measurements

Both the point-measurement function and the probing scan mode were used for the dimensional measurements to obtain superior accuracy. As shown in Figure 3(b), the method of fixture positioning limits the probe's access to the lower face of the cube. Consequently, to avoid errors caused by restricted accessibility and to maintain measurement precision, the base of the part was analyzed using two distinct planes, determined in separate positions.

Figure 4 presents an example of a report generated by the coordinate measuring machine, including the measurement paths, evaluated surfaces, and the deviation values determined for flatness, parallelism, and perpendicularity. The software representation illustrates how the measurement points were acquired and the distribution of deviations across the analyzed surfaces.

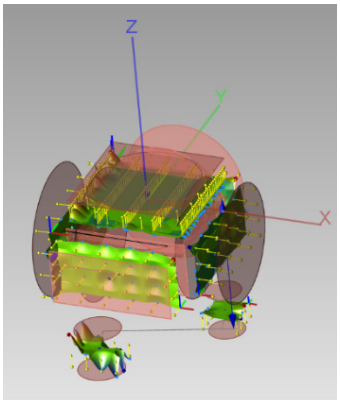

Figure 4. Example of a CMM report showing measurement paths, evaluated surfaces, and the distribution of flatness, parallelism, and perpendicularity deviations

In the graphical analyses presented in the results section, the mean values obtained from the five measurements performed on each of the five specimens corresponding to each infill density level were used. For a consistent interpretation of the data, Figure 5 presents the notation convention for the six analyzed planes:

A – front plane
B – top plane
C – right-side plane
D – left-side plane
E – bottom plane
F – rear plane

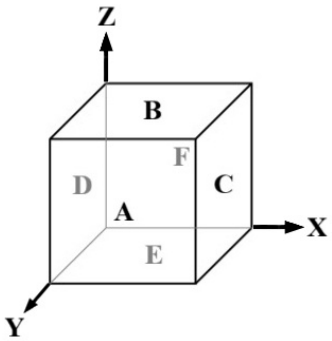

Figure 5. Notation convention for the six planes of the cubic test specimen

The X, Y, and Z axes illustrated in Figure 5 define the reference system of the specimen in its printing orientation. All specimens were measured while maintaining the same orientation as during fabrication, without reorientation relative to the coordinate measuring machine, in order to preserve the direct correspondence between printing directions and the measured dimensional deviations.

The measurements were carried out in the laboratory at 20 ± 1 °C, in accordance with the conditions recommended by the equipment manufacturer.

3. Results and Discussions

3.1. Dimensional Deviations

The dimensional deviations were automatically generated by the measurement software based on the values acquired by the CMM. Figure 6 (a–c) presents the mean deviations determined for the three analyzed pairs of planes (B–E, C–D, and A–F), which are relevant for the cubic geometry of the specimens.

For all pairs of planes, the deviations are negative, indicating a slight overall undersizing of the parts. However, the values are small, ranging from (–9.6 μm) to (–133 μm), which confirms good reproducibility of the FDM process for the analyzed geometry.

B–E distance (specimen height) – figure 6 a

The deviations are the smallest among all three measured directions. The maximum deviation, –41.4 μm, was recorded at 60% infill, while the minimum deviation, –9.6 μm, occurred at 40% infill. No clear trend correlated with infill density was observed. This high stability along the vertical (Z) direction can be explained by the fact that the part height is directly controlled by the layer-by-layer deposition increment, which limits the lateral flow of the molten material, an effect that is more pronounced along the X and Y directions.

C–D distance – figure 6 b

The values are larger than those along the B–E axis, ranging from –70.6 μm (80% infill) to –125.6 μm (60% infill). As in the case of the B–E distance, no coherent trend of the deviations as a function of infill density can be identified. The fluctuations can be explained by non-uniform shrinkage during cooling and by variations in internal stiffness provided by the infill structure.

A–F distance – figure 6 c

This direction exhibits the most noticeable trend. The deviation values decrease gradually with increasing infill density, from –133 μm at 20% infill to –102.3 μm at 80% infill. The observed improvement results from the progressive structural stiffening of the specimens, which reduces deformation along the longitudinal direction. At 100% infill, a slight increase in deviation is observed, suggesting that increasing density does not guarantee continuous improvement, phenomenon also reported in the literature.

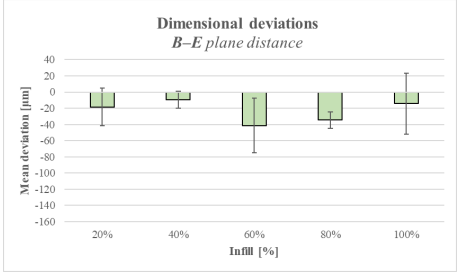

a

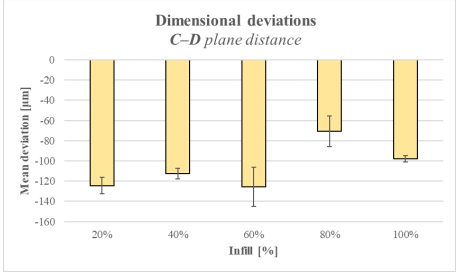

b

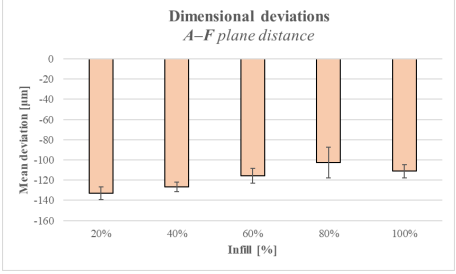

c

Figure 6. Mean dimensional deviations as a function of infill density

Overall, the dimensional deviations reveal different behaviors along the three analyzed directions. The deviations along the Z direction (B–E distance) are consistently the smallest, confirming the much stricter control of height in the FDM process, due to the layer-by-layer deposition and the absence of lateral material flow. In contrast, the horizontal directions (C–D and A–F) exhibit larger deviations, influenced by material shrinkage and the variable internal stiffness determined by the infill density. The only clear trend is observed along the Y direction (A–F distance), where increasing infill density leads, up to a certain point, to a reduction of deviations. Nevertheless, the behavior across the three axes suggests that the influence of infill density on dimensional accuracy is not uniform, depending significantly on the analyzed direction and on the way the material stabilizes during the cooling process.

3.2. Flatness Deviations

Figure 7 presents the flatness deviations for all six planes of the analyzed specimens. Overall, the values are low, not exceeding 90 μm, which indicates good geometric stability of the FDM-printed samples.

Planes A, C, and F exhibit a progressive increase in deviations as the infill density increases, reaching their maximum values at 80% infill, followed by a decrease at 100% infill. The minimum values are consistently recorded at 20% infill. This nonlinear evolution indicates that the relationship between infill density and flatness deviation is not monotonic. The increase in deviations up to 80% infill followed by a reduction at 100% may be influenced by the structural transition from a gyroid-filled configuration to a fully solid structure. This change may alter the overall stiffness and the redistribution of thermal and residual stresses within the part. However, internal stresses were not directly quantified in the present study, and therefore no specific causal mechanism is asserted.

Plane D, which contains the highest deviation in the entire dataset (87.6 μm at 80% infill), follows a similar pattern; although the variation is more pronounced. For this plane, the minimum deviation of 41.4 μm was recorded at 100% infill, confirming the trend toward geometric stabilization at very high densities.

Plane E shows a predominantly increasing behavior; however, the specimens at 40% infill deviate from this trend, exhibiting a higher value than those in the intermediate range. Even so, the maximum deviation is reached at 100% infill and the minimum at 20% infill, indicating a general correlation between increasing infill density and the intensification of stresses that affect flatness.

Plane B, the top surface of the specimen, does not exhibit a coherent variation with respect to infill density. The absence of a trend can be attributed to the fact that surface B represents the last deposited layer, which, typical of the FDM process, exhibits increased roughness and heightened sensitivity to the cooling and deposition features of the extruder.

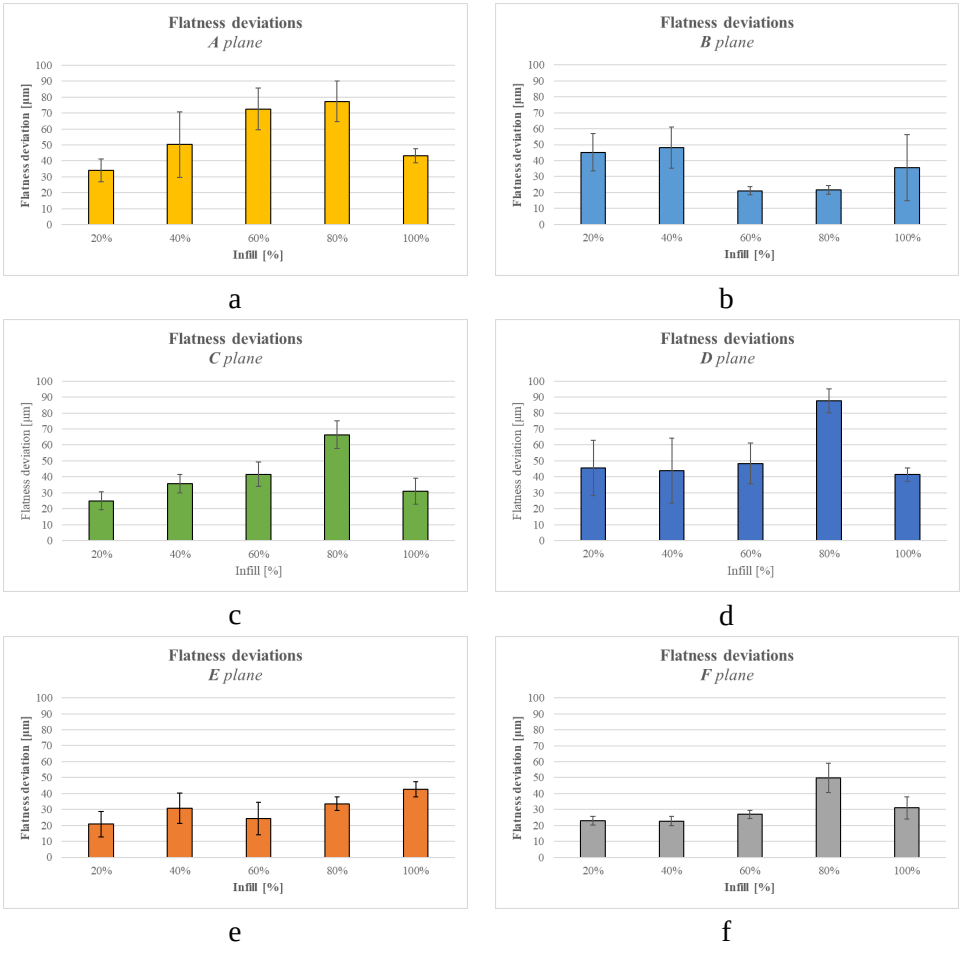

Figure 7. Influence of infill density on flatness deviations

Overall, the flatness deviations remain within low limits, yet clear tendencies can be observed on most planes: increasing infill density leads, up to a threshold of approximately 80%, to amplified deviations, followed by slight stabilization at 100% infill. The exceptions recorded on plane B and at certain intermediate levels (such as 40% infill on plane E) confirm that both local geometry and the sequence of deposited layers influence the way internal stresses affect surface flatness.

3.3. Parallelism Deviations

Figure 8 presents the parallelism deviations for the three pairs of planes of the analyzed specimens. Overall, the values are low, not exceeding 118.8 μm (B–E planes at 100% infill), which indicates good geometric stability of the FDM-printed parts.

For the A–F and C–D planes, a coherent evolution of the deviations is observed: they increase progressively with the infill density, reach a maximum at 80% infill, and subsequently decrease at 100% infill. The minimum deviations are consistently recorded at 20% infill, and the maximum deviations at 80% infill. This variation suggests that the internal stiffening induced by high infill densities may accentuate local deformations up to a certain threshold, followed by structural stabilization under full infill conditions.

In contrast, the parallelism of planes B–E (the upper and lower surfaces of the specimen) does not follow a clear trend with respect to infill density, with parallelism deviations reaching a maximum of 118.8 μm at 100% infill. When these results are correlated with the deviations of the B–E plane distance analyzed previously (which did not exceed a maximum value of –41.4 μm), it can be observed that global dimensional stability along the Z direction does not necessarily imply a similar evolution of parallelism.

This difference can be explained by the distinct geometric nature of the two quantities: the distance between planes represents an average dimensional deviation, whereas parallelism is sensitive to local variations in form and orientation. The upper plane (B), corresponding to the final deposited layer, exhibits increased roughness characteristic of the FDM process, while the lower plane (E), which is in contact with the build plate, is influenced by adhesion conditions and the surface characteristics of the plate.

Furthermore, as described in Section 2.2, the lower plane was determined as the mean of two separate plane evaluations performed in distinct positions imposed by fixture constraints, which may contribute to additional variability in the parallelism results.

Overall, the parallelism deviations remain low, with a clear evolution along the A–F and C–D directions, where increasing infill density leads to intensified deviations up to a maximum at 80% infill, followed by stabilization at 100%. The B–E planes do not exhibit a clear dependence on infill density, reflecting the strong influence of deposition characteristics on the upper plane and build-plate interaction on the lower plane—factors that attenuate the effect of internal stiffening.

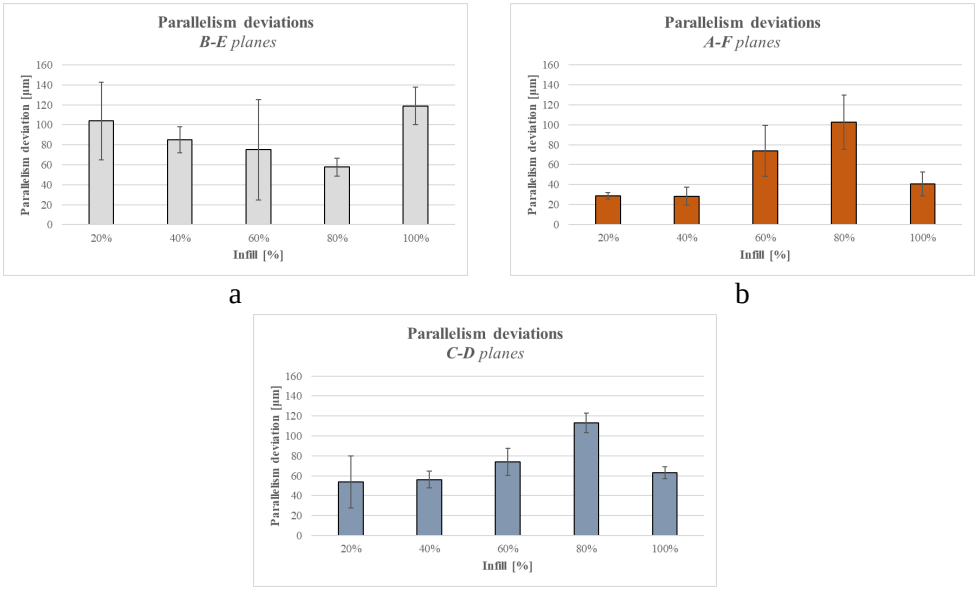

Figure 8. Parallelism deviations for the three analyzed plane pairs

3.4. Perpendicularity Deviations

Figure 9 presents the perpendicularity deviations for all analyzed plane pairs. Overall, the values are moderate, with a maximum of 228.8 µm for the perpendicularity of planes B–C at 20% infill, which also represents the largest deviation recorded in this measurement set.

However, the behavior of the deviations varies depending on the plane pair. For the B–F and F–D planes, the deviations increase with infill density, reaching a maximum at 80% infill and decreasing subsequently at 100% infill. The minimum values occur at 20% infill, suggesting that the progressive stiffening of the internal structure accentuates deviations up to a certain threshold, followed by geometric stabilization under full infill conditions.

The perpendicularities of the D–A, C–A, and F–C planes exhibit a similar trend, with an almost constant increase in deviations (though with local variations around 40% infill), the maxima being recorded at 80% infill, except for the F–C pair, where the maximum deviation occurs at 40% infill. At 100% infill, all these cases show a reduction in deviations.

For the E–F and E–D plane pairs, the deviations increase steadily with infill density, with the highest values reached at 100% infill and the lowest at 20%. This evolution indicates that the stiffening of the internal volume directly affects the maintenance of perpendicularity between planes, without stabilization at high infill levels.

Conversely, the perpendicularities of the B–C and D–B planes show an overall decreasing trend as infill increases, although the values obtained at 20% and 100% infill deviate from this evolution and stand out compared to the intermediate levels. These discrepancies can be explained by the increased sensitivity of these planes to variations in cooling and shrinkage, influenced both by internal stiffness and by the sequence of deposited layers.

For the B–A and E–C plane pairs, no clear correlation between infill density and perpendicularity deviations is observed. Both pairs include either the top or bottom plane of the specimen, surfaces that are inherently more sensitive to variations in the FDM process. The top plane corresponds to the final deposited layer, characterized by high roughness and low thermal stability, while the bottom plane is influenced by the contact conditions with the build plate, factors that can override the effect of infill density.

Overall, the perpendicularity deviations fall within moderate ranges but exhibit noticeable variations depending on the analyzed plane pair. Most pairs show an increase in deviations with rising infill density up to 60–80%, followed by a reduction at 100%, indicating a balance between internal stiffening and geometric stabilization. However, certain plane pairs, particularly those including the top or bottom surfaces of the part, do not follow a clear trend, being strongly influenced by FDM process-specific characteristics and the layer-by-layer deposition phenomenon.

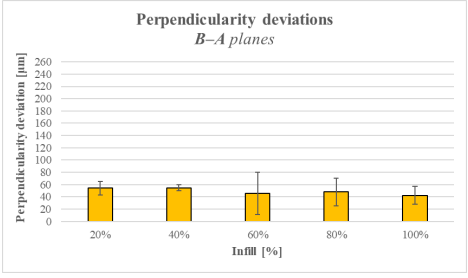

a

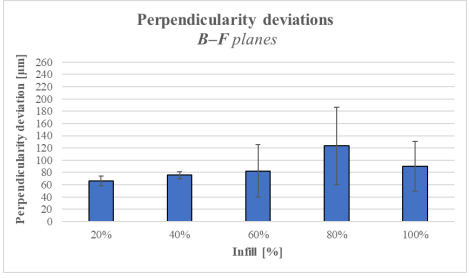

b

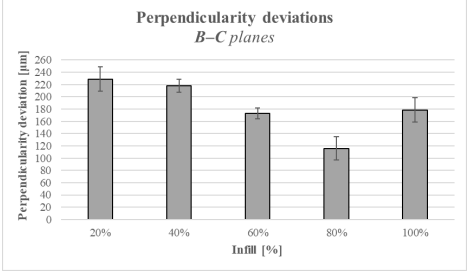

c

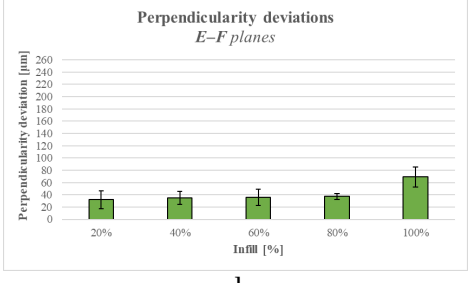

d

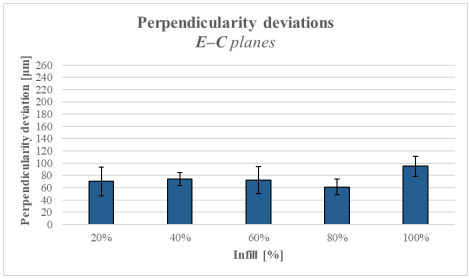

e

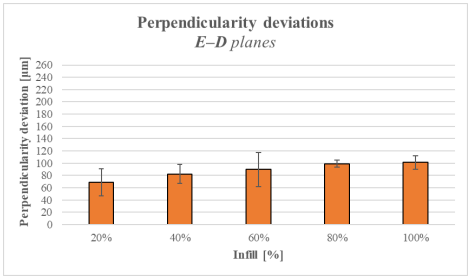

f

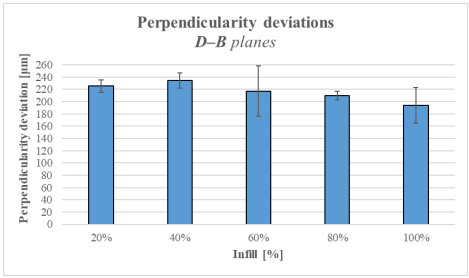

g

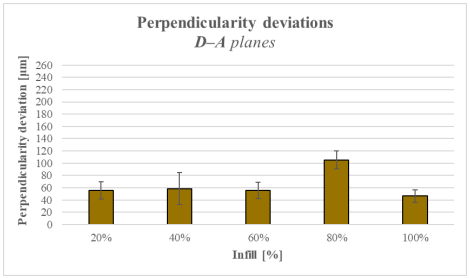

h

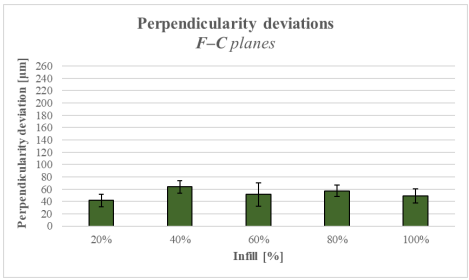

i

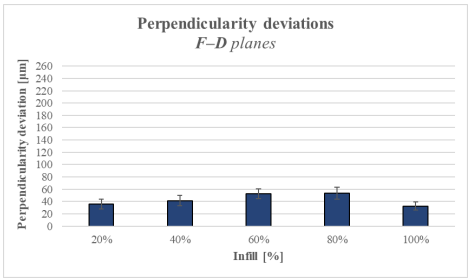

j

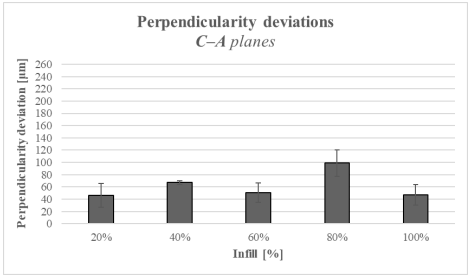

k

Figure 9. Perpendicularity deviations for the analyzed plane pairs

3.5. Variation of Mass and Printing Time

The influence of infill density is reflected not only in geometric deviations but also in production costs, since both the mass of material used and the required printing time are directly dependent on the amount of material deposited inside the part. The data regarding printing time and estimated material mass were collected from the Creality Print software used to generate the G-code for each specimen. Figures 10a and 10b present the variation of mass and printing time as a function of infill density.

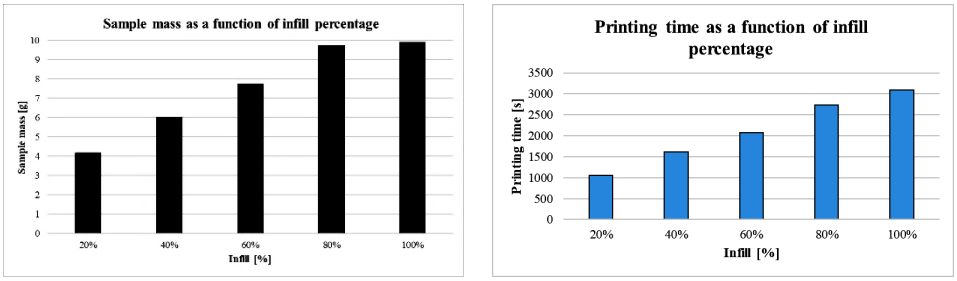

a b

Figure 10. Influence of infill density on specimen mass and printing time

A linear increase in specimen mass is observed, from 4.17 g at 20% infill to 9.86 g at 100% infill. This evolution is expected, given that the infill corresponds to the internal volume of the part, and increasing its density directly results in a larger amount of extruded material.

The printing time follows the same trend, increasing from 1060 s at 20% infill to 3089 s at 100% infill. As the infill density increases, the extruder must follow a larger number of internal paths, which extends the printing time and, consequently, the energy consumption of the process.

These results highlight that the choice of infill density has a direct impact on the overall production cost. A high infill density provides superior internal stiffening but requires both increased material consumption and significantly longer production times. Therefore, the infill level must be selected according to the functional requirements of the part (whether mechanical or geometric) to achieve an optimal compromise between performance, accuracy, and cost.

4. Conclusion

The study analyzed the influence of infill density on the dimensional, flatness, parallelism, and perpendicularity deviations of cubic specimens fabricated using FDM technology, employing five infill levels (20–100%). The obtained results allowed us to formulate the following conclusions:

- Dimensional deviations were negative and remained within relatively small limits (below –140 μm), without showing a clear dependence on infill level for all analyzed directions. Only for the A–F distance was a gradual improvement observed as infill increased up to 80%.
- Flatness deviations exhibited moderate increases for planes A, C, D, and F in the 20–80% infill range, followed by a decrease at 100%. The top (B) and bottom (E) planes showed irregular behavior, most likely due to the characteristic roughness of the final printed layer and the non-uniform adhesion to the build plate, which makes it difficult to identify a general infill-dependent trend.
- Parallelism deviations showed an increasing trend up to 80% infill for the A–F and C–D plane pairs, followed by a decrease at 100%. In contrast, the B–E pair did not show a consistent influence of infill density, suggesting that the top and bottom surfaces are more affected by the deposition characteristics of the final layers than by the internal structure of the part.
- Perpendicularity deviations displayed diverse behaviors without a unified trend. Some plane pairs (B–F, F–D) exhibited progressive increases in deviations up to 80% infill, followed by decreases at 100%, while others (E–F, E–D) showed an almost linear increase across the entire analyzed range. The B–C and D–B pairs showed decreasing deviations as infill increased, but the extreme values at 20% and 100% deviated from the general trend, indicating localized instabilities.
- Printing time and specimen mass increased linearly with infill density, confirming that higher densities involve greater material consumption and longer fabrication times. This trend must be considered when optimizing production costs.

Overall, the results indicate that infill density does not exert a strong or systematic influence on the geometric accuracy of the small-sized parts analyzed in this study. Instead, the observed effects are moderate, selective, and dependent on the orientation of the surfaces.

Given these findings, future research directions will include the fabrication of significantly larger parts, for which the effects of infill density on thermal stability, shrinkage, and geometric distortions may become more pronounced. Additionally, extending the investigation to mechanical testing and incorporating different infill patterns could contribute to the development of clearer predictive models regarding the geometric behavior of PLA in FDM processes.

References

1 Ardeljan D.D., Frunzaverde D., Cojocaru V., Turiac R.R., Băcescu N., Ciubotariu C.R., Mărginian G., The Impact of Elevated Printing Speeds and Filament Color on the Dimensional Precision and Tensile Properties of FDM-Printed PLA Specimens, *Polymers*, 17(15), 2025.

2 Cojocaru V., Turiac R.R., Frunzaverde D., Trișcă G., Băcescu N., Mărginian G., Effect of the Printing Scenario on the Dimensional Accuracy and the Tensile Strength of Different Colored PLA Specimens Produced by Fused Deposition Modeling, *Applied Sciences*, 14(17), 2024.
3 Frunzăverde D., Cojocaru V., Băcescu N., Ciubotariu C.-R., Micloșină C.-O., Turiac R.R., Mărginian G., The Influence of the Layer Height and the Filament Color on the Dimensional Accuracy and the Tensile Strength of FDM-Printed PLA Specimens, *Polymers*, 15(10), 2023.
4 Khan S.F., Zakaria H., Chong Y.L., Saad M.A., Basaruddin K., Effect of Infill on Tensile and Flexural Strength of 3D Printed PLA Parts, *IOP Conference Series: Materials Science and Engineering*, 429, 2018.
5 Abdulridha H., Abbas T., Analyzing the Impact of FDM Parameters on Compression Strength and Dimensional Accuracy in 3D Printed PLA Parts, *Engineering and Technology Journal*, 41(12), 2023, pp. 1611–1626.
6 Dave H.K., Patadiya N.H., Prajapati A.R., Rajpurohit S.R., Effect of Infill Pattern and Infill Density at Varying Part Orientation on Tensile Properties of Fused Deposition Modeling-Printed Poly-Lactic Acid Part, *Proceedings of the Institution of Mechanical Engineers, Part C: Journal of Mechanical Engineering Science*, 235(10), 2019, pp. 1811–1827.
7 Kadhum A.H., Al-Zubaidi S., AlKareem S.S., Optimization of Mechanical Properties and Surface Characteristics of PLA+ 3D Printing Materials, *International Journal of Chemical Engineering*, 2023.
8 Moradi M., Rezayat M., Rozhbiany F.A.R., Meiabadi S., Casalino G., Shamsborhan M., Bijoy A., Chakkingal S., Lawrence M., Mohammed N., Karamimoghadam M., Correlation between Infill Percentages, Layer Width, and Mechanical Properties in Fused Deposition Modelling of Poly-Lactic Acid 3D Printing, *Machines*, 11(10), 2023.
9 Öteyaka M.Ö., Aybar K., Öteyaka H.C., Effect of Infill Ratio on the Tensile and Flexural Properties of Unreinforced and Carbon Fiber-Reinforced Polylactic Acid Manufactured by Fused Deposition Modeling, *Journal of Materials Engineering and Performance*, 30(7), 2021, pp. 5203–5215.
10 Rismalia M., Hidajat S.C., Permana I.G., Hadisujoto B., Muslimin M., Triawan F., Infill Pattern and Density Effects on the Tensile Properties of 3D Printed PLA Material, *Journal of Physics: Conference Series*, 1402(4), 2019.
11 Alafaghani A., Qattawi A., Investigating the Effect of Fused Deposition Modeling Processing Parameters Using Taguchi Design of Experiment Method, *Journal of Manufacturing Processes*, 36, 2018, pp. 164–174.
12 Abas M., Habib T., Noor S., Salah B., Zimon D., Parametric Investigation and Optimization to Study the Effect of Process Parameters on the Dimensional Deviation of Fused Deposition Modeling of 3D Printed Parts, *Polymers*, 14(17), 2022.

13 Zonoobi M.A., Haghshenas Gorgani H., Javaherneshan D., Experimental Investigation and Multi-Objective Optimization of FDM Process Parameters for Mechanical Strength, Dimensional Accuracy, and Cost Using a Hybrid Algorithm, *Scientia Iranica*, 2023.
14 Solouki A., Aliha M.R., Makui A., Choupani N., Seiti H., Analyzing the Effects of Printing Parameters to Minimize the Dimensional Deviation of Polylactic Acid Parts by Applying Three Different Decision-Making Approaches, *Scientific Reports*, 14(1), 2024.
15 Singh T.K., Birru A.K., Singh K.N., Optimizing the Printing Parameters for Dimensional Accuracy of Distal Femur Bone by Using Taguchi's Method, *Journal of Engineering and Applied Science*, 71(1), 2024.
16 Galetto M., Verna E., Genta G., Effect of Process Parameters on Parts Quality and Process Efficiency of Fused Deposition Modeling, *Computers & Industrial Engineering*, 156, 2021.
17 Gunes S., Ulkir O., Kuncan M., Application of Artificial Neural Network to Evaluation of Dimensional Accuracy of 3D-Printed Polylactic Acid Parts, *Journal of Polymer Science*, 62(9), 2024, pp. 1864–1889.
18 Vălean C., Marşavina L., Linul E., Compressive Behavior of Additively Manufactured Lightweight Structures: Infill Density Optimization Based on Energy Absorption Diagrams, *Journal of Materials Research and Technology*, 33, 2024, pp. 4952–4967.
19 Miron I., Vălean C., Linul E., Infill Density Effect on the Flexural Behavior of FFF-Based AM Polylactic Acid Parts, *Materiale Plastice*, 62(3), 2025, pp. 1–9.

Addresses:

· Eng. Raul-Rusalin Turiac, PhD Candidate, Mechanical Engineering Doctoral School, Babes-Bolyai University,
Traian Vuia Square 1–4, 320085 Reșița, Romania
raul.turiac@ubbcluj.ro
· Assoc. Prof. Dr. Eng. Habil. Zoltan-Iosif Korka, Mechanical Engineering Doctoral School, Babes-Bolyai University,
Traian Vuia Square 1–4, 320085 Reșița, Romania
zoltan.korka@ubbcluj.ro
(**corresponding author*)
· Eng. Alexandra-Teodora Aman, PhD Candidate, Mechanical Engineering Doctoral School, Babes-Bolyai University,
Traian Vuia Square 1–4, 320085 Reșița, Romania
alexandra.aman@ubbcluj.ro

· Eng. Mihael Magda, PhD Candidate, Mechanical Engineering
Doctoral School, Babes-Bolyai University,
Traian Vuia Square 1–4, 320085 Reșița, Romania
mihael.magda@ubbcluj.ro

STUDIA UNIVERSITATIS BABEŞ-BOLYAI
Engineering 70(1) 2025 DOI: 10.24193/subbeng.2025.4

On the Dynamics of 3D-printed Gears with Lattice Structure

Mihael Magda, Zoltan-Iosif Korka*, Raul-Rusalin Turiac

Abstract. *The research investigates the integration of different lattice structures into gear design by applying them to the infill zone, which is located between the hub and rim of the gear. 3D models of the gears with varying lattice structures were created, and these gears were then constrained to a shaft for simulation purposes. Using the SolidWorks simulation module, a study was conducted to determine the interactions of natural frequencies, and the results were investigated. Gear variants V1-4 presented a good balance between mass reduction and higher stiffness, displaying higher natural frequencies overall, where these deformations manifest, in comparison to the original structure V0.*

Keywords*: natural frequency, SolidWorks, lattice structures, additive manufacturing, helical gears.*

1. Introduction

Gears are mechanical parts that use meshing teeth to transfer torque and rotational motion between shafts. Vibrations and noises that accompany their operation are mostly caused by wear, imbalances, misalignments, manufacturing errors, and variations in mesh stiffness [1]. Using lattice structures in the gear body's construction is one method of dampening vibration in gear systems.

The integration of lattice structures into gear design marks a significant advancement in mechanical engineering, fuelled by progress in additive manufacturing (AM) and topology optimization. This literature review explores the evolution, design principles, manufacturing methods, and performance characteristics of lattice-structured gears. The review shows that lattice-bodied gears have progressed from conceptual studies driven by topology to experimental demonstrators made possible by AM. Additionally, there is an increasing theoretical understanding of lattice topology, mechanics, and data-driven performance prediction, which informs optimization strategies and applications in the aerospace and automotive sectors.

Traditional gear design has typically focused on mechanical strength and durability [2], often at the expense of increased weight from solid metal structures. However, the advent of additive manufacturing technologies and advanced computational design methods has created new opportunities for producing lightweight, high-performance gears by incorporating lattice structures. These lattice structures, known for their periodic cellular designs, provide exceptional strength-to-weight ratios and can be customized to meet specific mechanical requirements, all while significantly reducing material usage [3].

The concept of lattice-structured gears combines several technological advances: topology optimization algorithms that identify the optimal distribution of materials, additive manufacturing processes that can create complex internal geometries, and advanced computational methods for predicting and optimizing lattice performance. This interdisciplinary approach has led to the development of gear systems that challenge conventional design paradigms and provide new solutions for weight-sensitive applications in aerospace, automotive, and other industries [4].

The use of topology optimization in gear design gained significant attention around 2018, when researchers developed workflows that treated the gear body as a design domain while keeping the geometries of the teeth and hub fixed during the optimization process. This approach acknowledged that while gear teeth must adhere to precise geometric tolerances for proper meshing, there are considerable opportunities for material reduction and structural optimization in the gear body [5].

Ramadani et al. conducted early research on topology optimization for gear bodies, establishing a foundational methodology for the development of lattice gears. These initial studies primarily aimed to reduce mass and minimize vibration through strategic material removal, thereby paving the way for more advanced lattice-based approaches.

The transition from conceptual topology optimization to practical lattice implementation become possible by advancements in additive manufacturing, particularly in selective laser melting (SLM) technology. Subsequent research led to the development of cellular lattice gears produced through SLM and other additive manufacturing methods. These gears have been experimentally shown to achieve measurable reductions in mass and changes in vibration and strain behaviour compared to traditional spur gears [6], [7].

The experimental demonstrations played a vital role in validating computational predictions and uncovering the practical challenges of manufacturing complex lattice structures. This work highlighted significant discrepancies between idealized computational models and the actual components produced, emphasizing the need to consider manufacturing constraints during the design process.

As lattice manufacturing technologies have matured, several comprehensive reviews and surveys have consolidated knowledge on classification schemes, additive manufacturing (AM)-based design methods, and performance metrics that are ready

for application in lattice structures. This phase of consolidation has been crucial for promoting wider adoption across various industrial sectors and for establishing standardized approaches to the design of lattice gear [6-8].

Recent advancements have led to the development of parametric plate lattices and shape-optimized plate families, which broaden the range of achievable mechanical properties. These sophisticated lattice configurations can be designed to display either isotropic or anisotropic stiffness characteristics, allowing the lattices to approach the theoretical stiffness limits for a given density.

The flexibility of parametric lattice families allows designers to customize gear body properties according to specific loading conditions and operational requirements. This capability is especially valuable in applications where directional loading or specific vibration characteristics are critical design factors [9], [10].

Research on fused filament fabrication (FFF) of polymer lattice structures has yielded valuable insights into the relationships between manufacturing parameters and mechanical properties. Compression tests conducted on FFF-printed gyroid, diamond, and octet lattices have demonstrated that factors such as cell size, strut/wall thickness, and layer thickness significantly influence strength and deformation capacity [10].

Although polymer lattices may not be ideal for high-load gear applications, the insights gained from polymer studies have enhanced the understanding of manufacturing-property relationships that apply more broadly to lattice manufacturing processes [11]. This study serves as an extension of our team's prior research efforts [12], [13].

2. Materials and Methods

Lattice structures are systematically categorized based on their topology and deformation mechanisms, which significantly influence their mechanical behaviour. The main topological classifications include strut-based lattices, surface or shell lattices, hollow-strut configurations, triply periodic minimal surfaces (TPMS) like gyroid structures, and plate lattices [8], [9]. Each class of topology displays unique mechanical properties that make them suitable for various applications.

A helical gear (V0) with the relevant geometrical details shown in Table 1 was used as the basis of the initial design, while the lattice structures (infill patterns) were set in four distinctive designs (V1-V4).

The helical gear's crown and hub were effectively designed with a 100% solid infill, focusing modifications specifically on the region between diameters Ø45 mm and Ø130 mm. Utilizing SolidWorks, all geometries were crafted with direct modelling techniques and standard features, such as Extruded Boss/Base and Circular Pattern, across various iterations, except for the initial version (V0).

Table 1. Relevant parameters of the base helical gear design.

Parameters	Symbol [m.u.]	Value
Gear module	m_n [mm]	2
Teeth number	z	75
Gear width	b [mm]	17
Helix angle	β [°]	10
Pressure angle	α [°]	20
Profile shift coefficient	x	-0.659
Tip diameter	d_a [mm]	153.496
Reference diameter	d [mm]	152.314
Root diameter	d_f [mm]	144.078
Gear Hub distance	d_h [mm]	45
Gear rim distance	d_r [mm]	130
Material	C45-EN 10083-2	

The first variant (V1- Figure 1) was developed by initially sketching a rib and then applying a circular pattern multiplication. The rib thickness was selected at 0.8 mm, whereas the number of multiplication instances is 72, at a total angle of 360°.

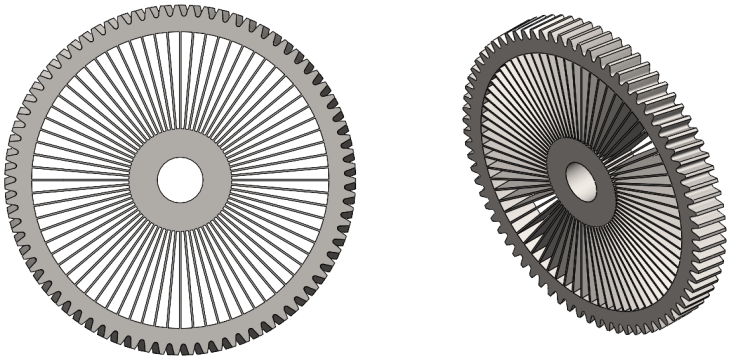

a. b.

Figure 1. V1 gear model with linear pattern infill (a. front view; b. isometric view)

The second variant (V2- Figure 2) was developed by positioning two circle arcs with an equal radius of R60 at a 45° from the line of reference. Employing the circular pattern multiplication feature, the infill pattern was obtained. The rib thickness was selected at 0.8 mm whereas the number of instances multiplicated was 72 at a total angle of 360°.

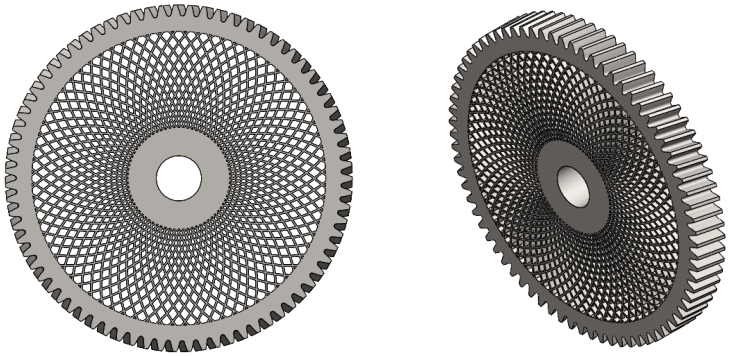

a. b.

Figure 2. V2 gear model with circular arc pattern infill
(a. front view; b. isometric view)

For the third variant (V3-Figure 3), 0.8 mm thick rib was established, where the chords intersect at 45º. By applying the circular pattern multiplication feature, the infill pattern was created. The number of instances multiplied was 72, with a total angle of 360°.

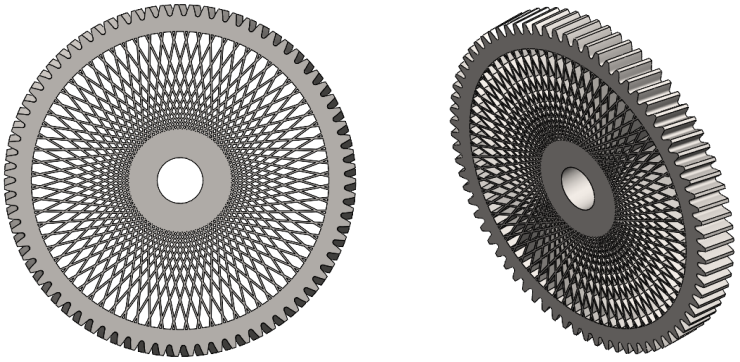

a. b.

Figure 3. V3 gear model with 45°-line intersection infill
(a. front view; b. isometric view)

The fourth variant (V4-Figure 4) features a honeycomb infill design, consisting of regular hexagonal cells. The wall thickness of these cells is 0.8 mm, and the diameter of the circle inscribed within each hexagon measures 3 mm. The infill pattern was created by applying a circular pattern multiplication feature following the initial sketch. The number of instances multiplied was 72 with a 360° total angle.

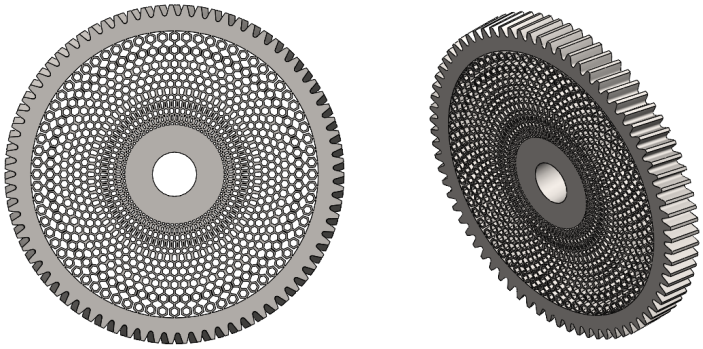

a. b.

Figure 4. V4 gear model with honeycomb pattern infill
(a. front view; b. isometric view)

For the assessment of the five geometries presented above, finite element analysis and simulations were performed using the Frequency Analysis module, available in the SolidWorks 2024 software [14]. This approach provides valuable insights into the performance characteristics and design optimization of the gears.

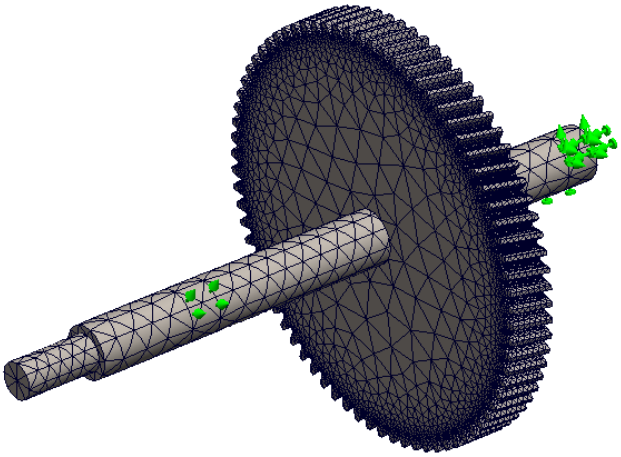

Figure 5. Boundary conditions and the mesh applied in the frequency analysis

The natural frequency analysis for the five geometries was conducted on the helical gear–shaft assembly (Figure 5). The gear wheels were fixed on the shafts by means of press fit. Moreover, appropriate bearing constraints were applied to the shaft.

Table 2. Mesh parameters of the V0-4 gear design.

Details	V0	V1	V2	V3	V4
Mesh type	Solid Mesh				
Mesher used	Blended curvature-based mesh				
Jacobian points for High quality mesh	16				
Max. element size [mm]	14.2549	16.008	19.5354	18.9333	19.6357
Min. element size [mm]	0.719224	0.8004	0.976768	0.946667	0.981785
Maximum Aspect Ratio	5.4613	68.218	85.814	125.97	274.89
Total Nodes	250344	191562	236162	210320	277828
Total Elements	166459	120585	140782	125768	156022

The details regarding the mesh parameters applied to the five gear designs (V0-V4) are presented in Table 2, where the Jacobian points value of 16 indicate fewer sharp edges and/or curved extremities for the generated meshes.

3. Results and Discussion

Table 3 illustrates the variations in mass for the analysed gears. All four lattice structure geometries demonstrate significant mass decreases Notably, the most substantial mass reduction was observed in the V1 and V3 geometries when compared to the original geometry (V0).

Table 3. Variations of the mass for the V0-V4 gear models.

Model code	Mass of the gear (g)	Variation of mass versus V0 model (%)
V0	2266.44	0.00
V1	1041.91	-54.03
V2	1398.08	-38.31
V3	1329.37	-41.35
V4	1397.24	-38.35

Whereas in Figure 6, we can observe the variation of mass through a visual representation of these values.

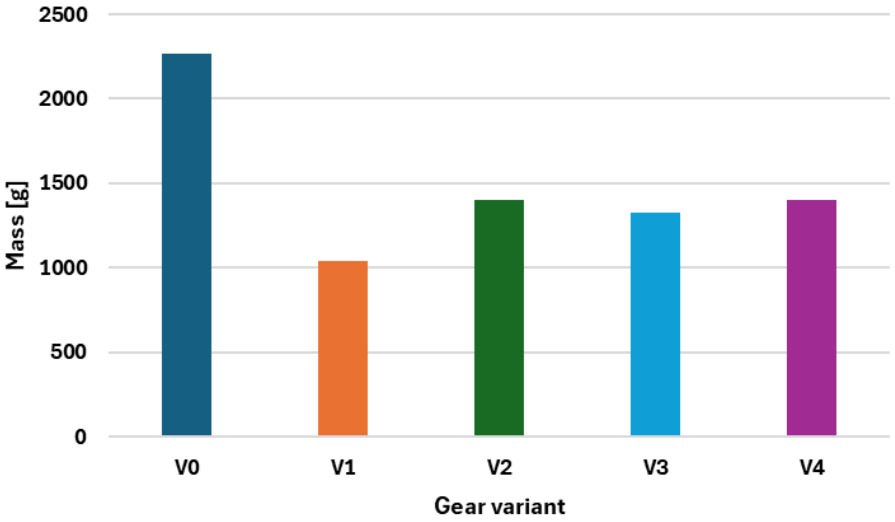

Figure 6. Visual representation of mass variation for the V0-V4 gear models

Table 4 displays the natural frequencies for the first six vibration modes of the analysed geometries, highlighting the effect of geometric modifications on vibrational behaviour.

Table 4. Natural frequency comparison between the five models.

Model code	Natural frequencies [Hz]					
	Mode 1	Mode 2	Mode 3	Mode 4	Mode 5	Mode 6
V0	283.17	912.44	913.15	1166.50	1169.10	2227.40
V1	173.45	1196.80	1198.20	1443.90	1445.70	1773.70
V2	348.74	1113.50	1114.50	1374.60	1375.30	2184.40
V3	357.71	1139.80	1140.30	1399.40	1401.20	2217.70
V4	344.06	1106.90	1108.60	1353.80	1355.10	2187.80

Notably, there are significant differences between the original and modified geometries, as shown in Figure 7, where the modified versions show higher overall frequency values. This trend is directly linked to increased structural stiffness; stiffer configurations resist deformation more effectively, resulting in higher natural vibration frequencies.

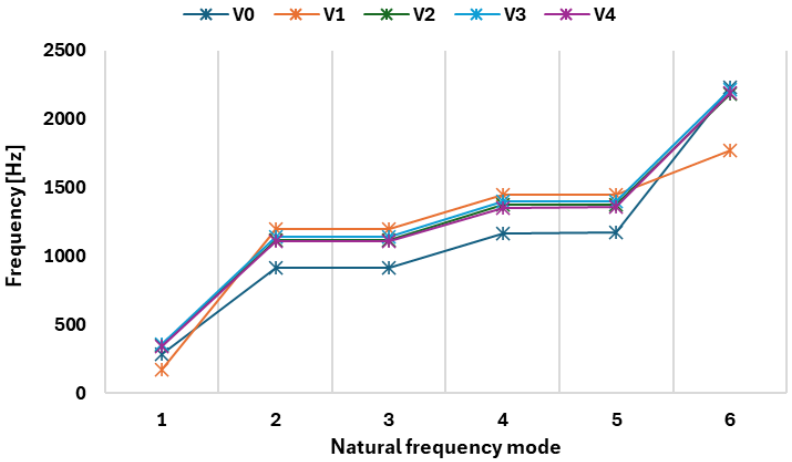

Figure 7. Visual comparison between the five models

Figures 8-12 illustrate the shapes associated with the first six vibration modes for the gear variants V0–V4. These mode shapes reveal that geometries with lattice infill structures (V1–V4) exhibit similar deformation patterns, indicating a consistent vibrational response due to their periodic lattice architecture.

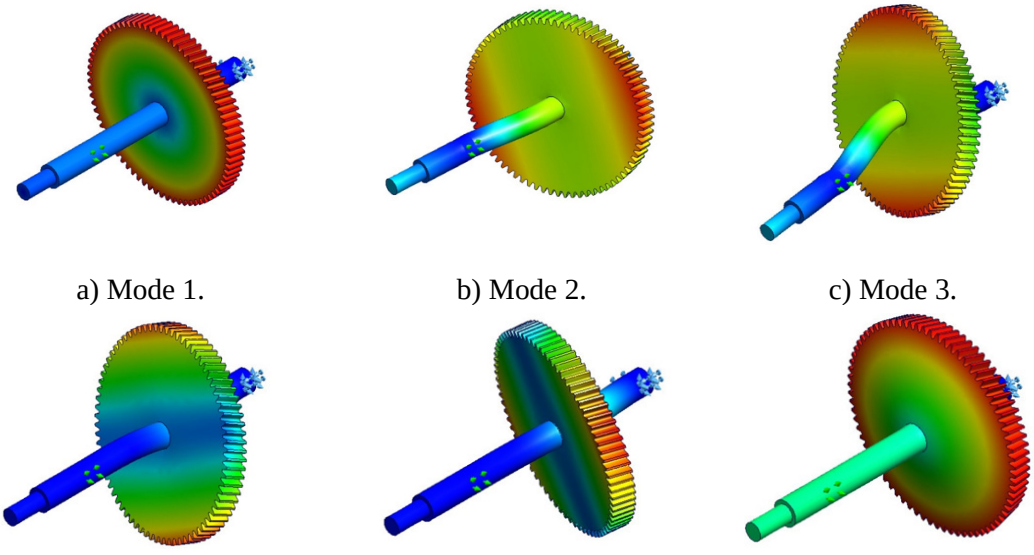

a) Mode 1. b) Mode 2. c) Mode 3.

d) Mode 4. e) Mode 5. f) Mode 6.

Figure 8. First six mode shapes for the V0 gear design

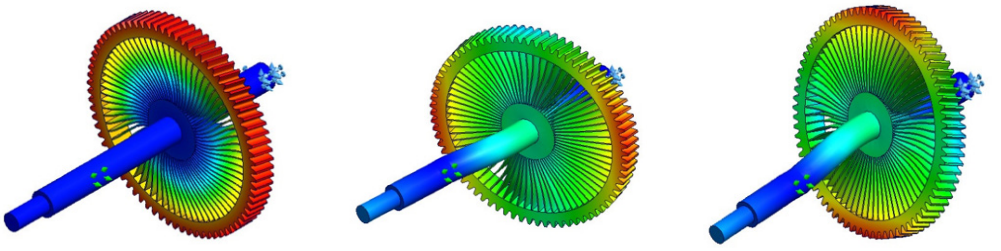

a) Mode 1. b) Mode 2. c) Mode 3.

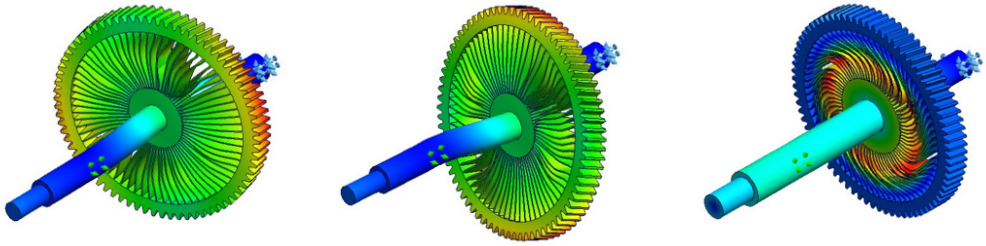

d) Mode 4. e) Mode 5. f) Mode 6.

Figure 9. First six mode shapes for the V1 gear design

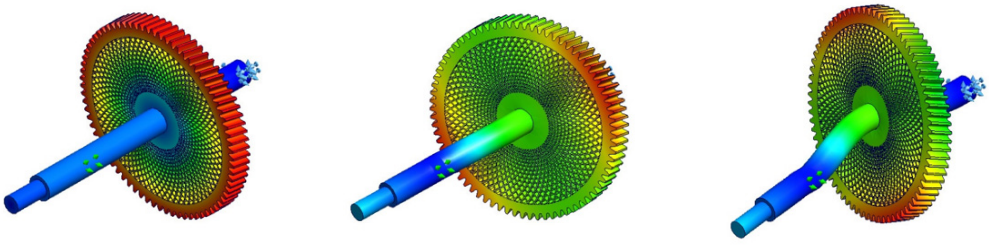

a) Mode 1. b) Mode 2. c) Mode 3.

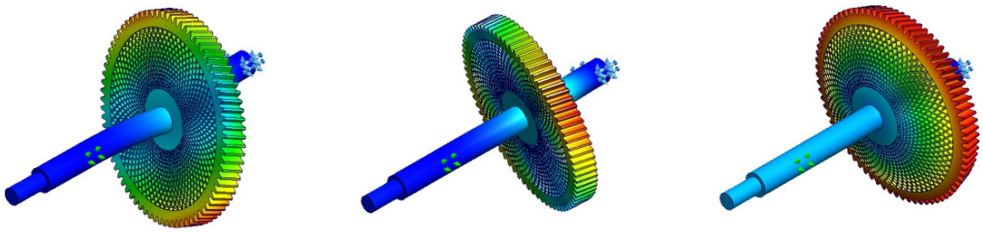

d) Mode 4. e) Mode 5. f) Mode 6.

Figure 10. First six mode shapes for the V2 gear design

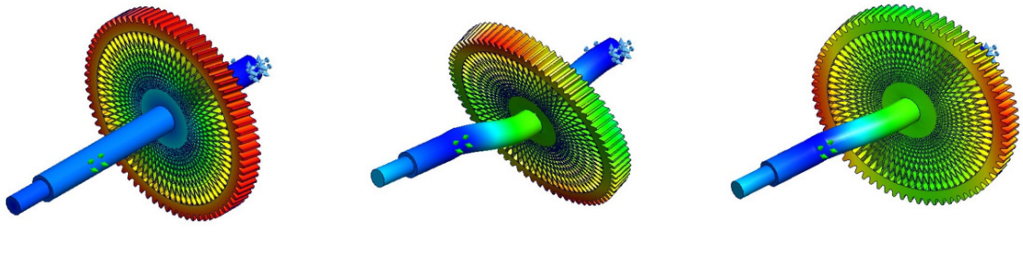

a) Mode 1. b) Mode 2. c) Mode 3.

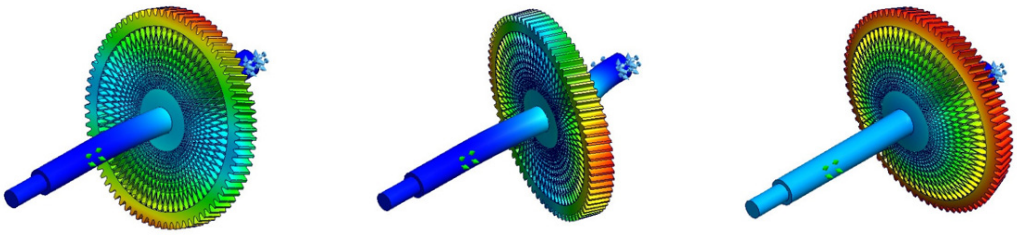

d) Mode 4. e) Mode 5. f) Mode 6.

Figure 11. First six mode shapes for the V3 gear design

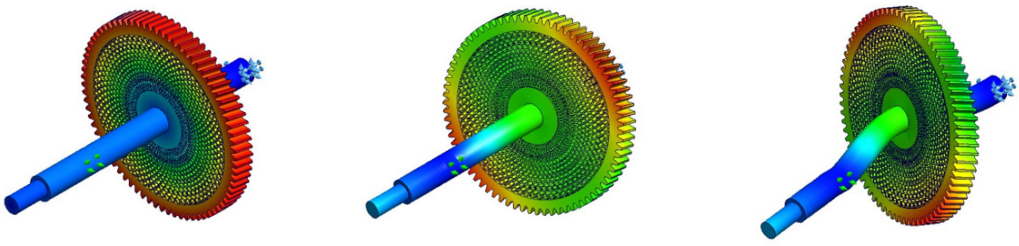

a) Mode 1. b) Mode 2. c) Mode 3.

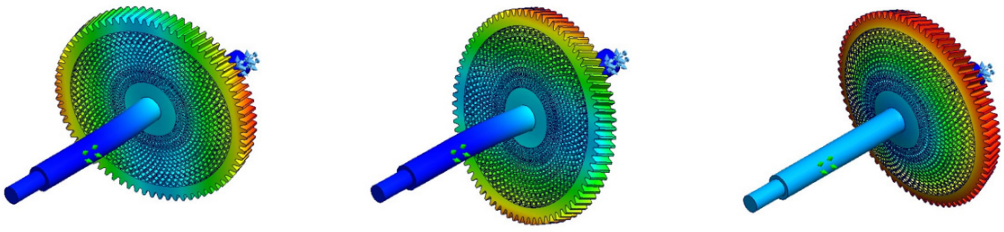

d) Mode 4. e) Mode 5. f) Mode 6.

Figure 12. First six mode shapes for the V4 gear design

In contrast, as it can be observed in Table 4, the original geometry (V0) displays distinct deformation patterns, highlighting the impact of internal structure on vibrational behaviour.

The much lower value of the eigenfrequency corresponding to the vibration mode 1 obtained in the V1 variant, compared to the V2-V4 designs, is explained by the fact that vibration mode 1 is a purely torsional one and V1 is the lattice structure that gives the lowest torsional rigidity. As in modes 2 and 3, bending vibrations are predominant, the deviation of the natural frequencies proper to the 4 variants of lattice structures is much smaller.

The use of optimized infill patterns in the internal structure of additively manufactured helical gears offers the possibility of improving stiffness and increasing natural frequencies while reducing gear mass.

4. Conclusion

The research aimed to investigate the impact of various lattice infill designs on gear stiffness and their effects on total gear mass.

The natural frequencies of the first six vibration modes for the analysed geometries highlight how geometric modifications influence vibrational behaviour. The modified versions exhibited higher overall frequency values, which is directly linked to increased structural stiffness, as stiffer configurations are better at resisting deformation.

Incorporating lattice infill patterns in the internal structure of additively manufactured helical gears not only enhances their stiffness but also increases the natural frequencies at which deformations begin to occur, all while significantly reducing the overall mass of the gears. The findings suggest that using lattice infills in gear design results in favourable stiffness-to-mass ratios.

Overall, this study builds on previous research in the field, laying the foundation for future improvements and optimizations. Future research directions aim to investigate more complex cellular structures, capable of providing both an increased torsional rigidity and to serve as vibration absorber for the gear dynamics.

References

1 Korka Z.I., Vela I., Design and execution of a test rig for studying the vibrations of a gearbox, *Annals of "Eftimie Murgu" University from Resita*, 15(1), 2008, pp. 131-140.

2 Korka, Z. I., Cojocaru, V., Miclosina, C. O., Modal-based design optimisation of a gear box housing, *Romanian Journal of Acoustics and Vibration*, 16(1), 2019, pp. 58-65.

3 Ramadani, R., Pal, S., Belšak, A., et al., *Selective Laser Melting of a Ti-6Al-4V Lattice-Structure Gear: Design, Topology Optimization, and Experimental Validation*, Applied Sciences, 15(14), 2025, 7949.
4 Li, Y., Jiang, D., Zhao, R., et al., *High Mechanical Performance of Lattice Structures Fabricated by Additive Manufacturing*, Superalloys, 14(10), 2024, 1165.
5 Ramadani, R., Belšak, A., Kegl, M., et al., *Topology Optimization Based Design of Lightweight and Low Vibration Gear Bodies*, International Journal of Simulation Modelling, 17(1), 2018, 92-104.
6 Sur, A., & Darvekar, S., *Recent Advancements of Micro-Lattice Structures: Application, Manufacturing Methods, Mechanical Properties, Topologies and Challenges*, Arabian Journal for Science and Engineering, 2021, 46, 8513-8556.
7 *Topology optimization and additive manufacturing in producing lightweight and low vibration gear body*, International Journal of Advanced Manufacturing Technology, 2021, 115, 1639-1651.
8 Yang, S., Dai, N., & Cao, Q., *The Data-Driven Performance Prediction of Lattice Structures: The State-of-the-Art in Properties, Future Trends, and Challenges*, Aerospace, 12(5), 2025, 390.
9 Lu, L., 2023, Parametric plate lattices: *Modeling and optimization of plate lattices with superior mechanical properties*, Additive Manufacturing, 71, 103626.
10 Sharpe, C., & Seepersad, C. C., *Lattice Structure Optimization With Orientation-Dependent Material Properties*, Proceedings of the ASME International Design Engineering Technical Conferences, 2020.
11 Kara, H., & Uzun, M., *Farklı Dolgu Geometrilerine Sahip Dişli Çarklarda Ağırlığın Optimize Edilmesi*, Türk Doğa ve Fen Dergisi, 13(4), 2024, 180-190.
12 Cojocaru, V.; Frunzaverde, D.; Miclosina, C.-O. *On the Behavior of Honeycomb, Grid and Triangular PLA Structures under Symmetric and Asymmetric Bending*. Micromachines 2023, 14, 120.
13 Cojocaru, V., Miclosina C.O. & Korka Z.I., *Study of the dynamic behavior of gears with lattice structure body*, The 3rd International Conference on Mechanical System Dynamics, Sept 23rd– 27th, 2025, Cluj-Napoca, Romania.
14 Dassault Systems, Support Documentation, available online at: https://www.3ds.com/support/documentation/

Addresses:

· PhD. stud. eng. Mihael Magda, Doctoral School of Engineering,
Babeș-Bolyai University, Cluj-Napoca, Romania,
Piaţa Traian Vuia, no. 1-4,320085, Reşiţa
magda.mihael@ubbcluj.ro

· Associate Professor, PdD. Habil. eng. Zoltan-Iosif Korka, Department of Engineering Sciences, Faculty of Engineering, Babeș-Bolyai University Cluj-Napoca, Romania,
Piaţa Traian Vuia, nr. 1-4, 320085, Reşiţa
zoltan.korka@ubbcluj.ro
(*corresponding author)
· PhD. stud. eng. Raul- Rusalin Turiac, Doctoral School of Engineering, Babeș-Bolyai University, Cluj-Napoca, Romania,
Piaţa Traian Vuia, no. 1-4,320085, Reşiţa
raul.turiac@ubbcluj.ro

STUDIA UNIVERSITATIS BABEŞ-BOLYAI
Engineering 70(1) 2025 DOI: 10.24193/subbeng.2025.5

Grindability and Mineralogical Characterization of Ikpeshi Basalt for Effective Soil Amendment

Rasheed Ibrahim*, Akinbile Oluwakunmi Christopher, Babatunde Sunday Ewulo, Ayodele Olumuyiwa Owolabi, Sunday Adakole, Asishana Stanley Ajayi

Abstract. *This study assessed the grindability and mineralogical composition of basalt rock collected from Ikpeshi town, Edo State, Nigeria. Using the work index approach, its suitability as an amendment for agricultural soil was evaluated while calcite rock was used for comparison as the reference ore. The samples were crushed, milled, and pulverized to pass through a sieve of 1180µm, after which 100g portions were subjected to sieve analysis (1000–63µm) to establish data for their grindability potential. Results revealed a work index of 10.10 kWh/t for calcite and 18.722 kWh/t for Ikpeshi basalt, with actual grinding energy for basalt determined as 3.52 kWh. The elemental and chemical characterization of both rocks was carried out using the X-ray Fluorescence (XRF) and X-ray Diffraction (XR) approach, the mineralogical analysis revealed that the basalt rock contains minerals that are essential for improved soil fertility. The study highlights Ikpeshi basalt as a mineral resource with moderate grinding energy requirements and strong potential for sustainable use as a soil amendment.*

Keywords: *Grindability, Basalt, Sieve shaker, Comminution, Soil amendment.*

1. Introduction

Basalt is one of the most common types of volcanic rock on earth. It formed when low-viscosity lava cools quickly at or near the surface. These deposits are usually found at divergent plate borders, oceanic hotspots, and large igneous provinces (LIP). The Deccan Traps in India and the Columbia River Basalt Group in the United States are two of the most famous continental basalt formations. They were made during times of heavy volcanic activity that were connected to mantle plumes [1]. Basalt deposits

in the water are very common, especially near mid-ocean ridges, where new oceanic crust is always being made [2]. Basalt differs from other intrusive igneous rocks like gabbro due to its fine-grained texture and mineral composition, which mostly consists of pyroxene and plagioclase. These characteristics suggest fast cooling. Over time, these massive basalt flows can create plateaus and cover sizeable areas, causing major changes in the ecosystem and geology [3].

Minerals like calcium, magnesium, and potassium, which are necessary for plant growth, are abundant in basalt, a volcanic rock [4]. It has been demonstrated that applying basalt as a soil supplement increases soil fertility and boosts agricultural yields [5]. Particularly in tropical and subtropical areas where weathering has reduced nutrient levels, the mineral makeup of basalt can aid in restoring nutrient-deficient soils [6]. In recent years, there has been a growing interest in investigating basalt as a soil supplement, especially in areas where the soil quality is not ideal for agricultural output. Because of its grindability, basalt especially that from Nigeria's Ikpeshi region offers a rare chance to evaluate its potential as a useful soil amendment. This paper summarizes the body of knowledge regarding the use of basalt in agriculture, the characteristics of basalt that make it a useful soil amendment, and the techniques used to determine how grindable it is.

According to a study by [7], basalt greatly improves the soil's micronutrient availability, which supports better growth of plants. Furthermore, basalt is a useful amendment in areas with high acidity because of its alkaline composition, which can help neutralize acidic soils [8]. Basalt's potential advantages in sustainable agriculture are highlighted by its dual function as a pH balancer and a supplier of soil nutrients. The physical and chemical characteristics of basalt are primarily responsible for its efficacy as a soil amendment. According to [9], basalt's high specific surface area can increase its reactivity in soil conditions. Better contact with soil particles and microorganisms is made possible by this characteristic, which promotes nutrient exchange and enhances soil structure [10].

Furthermore, depending on its geological genesis, basalt's mineralogical makeup varies greatly, which may affect how efficient it is as an amendment. For example, zeolites can improve the capacity to contain nutrients and retain water in some basalt deposits [11]. Therefore, in order to ascertain whether Ikpeshi basalt is suitable as a soil amendment, a thorough examination of its mineralogical composition is required. The usefulness of basalt as a soil amendment is largely dependent on its grindability. For a material to be used effectively in agricultural activities, it must be easy to convert to a powder, which is known as its grindability [12]. Numerous investigations have studied the grindability of different geological materials; frequently use the Bond work index as a benchmark [13]. In the case of basalt, the texture, mineral composition, and existence of any secondary minerals can all affect its grindability [14]. There is a substantial vacuum in the research because Ikpeshi basalt's grindability and mineral composition has not been investigated or reported, determining the economic viability of using basalt deposit as a soil supplement requires an understanding of its grindability.

The grindability of geological materials has been evaluated using a variety of techniques. The Bond work index, which measures the energy needed to grind a material to a particular size, is most commonly calculated using ball mills [13]. Other methods include the use of laboratory-scale grinding tests and empirical models that correlate grindability with physical properties [15]. Other approaches to evaluating grindability have been made possible by recent technological developments in addition to these conventional methods. For example, more thorough understanding of the grinding process and the resulting particle size distribution can be obtained by the use of digital photography and particle size analysis [16]. These developments have the potential to improve the precision of grindability evaluations, yielding more trustworthy information for assessing Ikpeshi basalt.

It's also important to think about how using basalt as a soil amendment may affect the environment. Carbon emissions and habitat disruption are two ecological effects of basalt extraction and processing [17]. The advantages of better soil health and higher agricultural productivity exceeded these disadvantages when used sparingly [18].

The economic factors are equally significant. It is necessary to compare the cost-effectiveness of applying and grinding basalt as a soil amendment to alternative techniques for improving soil quality [19]. Local farmers and food security may greatly benefit from the potential for basalt deposits to offer a sustainable and reasonably priced source of soil amendment.

The potential advantages of basalt as a soil additive for increasing crop yields and soil fertility are highlighted. Ikpeshi basalt, particular its grindability aspect is underexplored, therefore, more study is required to determine whether it is suitable for use in agriculture. By analyzing the characteristics of Ikpeshi basalt and using proper approach to evaluate its grindability, this study aims to fill a critical gap in the literature and contribute to the sustainable use of local geological resources in agriculture.

2. Materials and Method

2.1. Materials

Materials used for this research are basalt rock sample sourced from Ikpeshi town in Edo State Nigeria, while reference mineral was found from the test ore over burden in the same site at Etsako West Local Government Council.

2.2. Methods

Fifty (50) kilograms of the basalt rock sample was collected from five (5) different pits at Ikpeshi quarry site located in Etsako West Local Government with coordinate 7.0084^0N, 6.0143^0E in Edo state, Nigeria. These samples were collected at a dimension of 5 meters length by 5 meters breadth and depth of 13 meters and above [20] with

a distance of 100 meters apart. The sourced samples were mixed thoroughly and homogenized to obtain a uniform sample using the cone and quartering method of sampling. The grab sampling method was used to collect ten (10) kilograms of calcite from each pit overburden. The lumpy basalt was crushed using a Yu Feng100 x 60 jaw crusher (model XL1349) and then ground using a ball mill (locally fabricated at Auchi Polytechnic) to a sieve aperture 1180 μm until 100% passing was obtained. Five hundred (500) grams of the ground Basalt was collected using Jones Riffle's random sampling methods and prepared for chemical characterization to determine their elemental compositions. Hundred (100) grams of the ground Basalt was charged into an array of sieves arranged in root two (√2) (that is, from 1000 – 63 μm) on a Jinling Ro–Tap automated sieve shaker machine (model 890212050023) and shook for 15 minutes after which the retained on each sieve were weighed and recorded as feed into a ball mill (Ft). Sample from this prepared sample was equally charged into a ball mill and ground for 20 minutes to obtain ball mill product from further size reduction. 100 grams of this ball mill product was equally charged into a set of sieves. Retained products on each sieve were weighed and recorded. From the Table, a log-log graph was used to plot the percentage of cumulative weight retained and passing against the sieve sizes in micrometers. These procedures were repeated for the reference mineral (calcite).

2.3. Bond's work index determination

Gaudin Schumann's expression is often used to derive a modified approach for calculating the work index of Ikpeshi Basalt, which resulted in an 80% passing rate. Gaudin Schumann's expression thus:

$$P(X) = 100(\frac{X}{K})\alpha^{i} \quad (1)$$

Where:
P(X) = Cumulative percentage passing
x = Particle size
k = Size modulus
a = Distribution modulus

$$\alpha = \frac{Log\ P(x_2) - P\ (x_1)}{Log\ (x_2) - PLog\ (x_1)} \quad (2)$$

$$\alpha = x_2 = \frac{(Px_2)^2}{(Px_1)^2} \times x_1 \quad (3)$$

$P(x_2)$ = Percentage Passing Size at 80 % passing
$P(x_1)$ = Percentage Passing Size before 80 % passing
x_1 = Sieve size before 80 % passing
$\alpha = (x_2)$ = Sieve sizes at 80 % passing

Net power required P (KWhr) = $\frac{(Ploaded - Pempty)\, x\, th}{Mass\ of\ feed\ (tonnes)}$ (4)

Ploaded is electric power required to grind loaded rock feed (KW)
Pempty is standard idling electric power required without rock feed (KW)th is grinding or operating time (hrs)
m is mass of rock grinded (tonnes)

The work index of Ikpeshi basalt was determined using

$$(\text{Wit}) = \frac{P}{10\,(\frac{1}{\sqrt{Pt}} - \frac{1}{\sqrt{Ft}})} \quad (5)$$

Energy used in comminution of Ikpeshi basalt was determined using

$$\text{Et} = \text{Wit}(\frac{10}{\sqrt{\text{Pt}}} - \frac{10}{\sqrt{\text{Ft}}}) \quad (6)$$

Wit = Work index of rock feed
Et = energy required, kWh
Ft = Sieve size of Basalt feed into ball mill, 80% passing through 100 μm
Pt = Sieve size of Basalt Product from the ball mill, 80% passing through 100 μm
Frs = Sieve size of Reference ore feed into ball mill, 80% passing through 100 μm
Prs = Sieve sive of Reference ore Product from ball mill, 80% passing through 100 μm [13, 21].

2.4. Results and Discussion

Table 1. Mineral Composition of Ikpeshi Basaltic Rock (%)

Location	SiO_2	Al_2O_3	Fe_2O_3	CaO	MgO	Na_2O	K_2O	SO_3	P_2O_5	TiO_2	LOI
Iesha Basalt	48.32	13.12	8.02	6.19	5.05	1.42	6.76	0.20	7.63	1.48	1.32

Table 2. X-ray Fluorescence Spectrometer (Chemical) Analysis of Ikpeshi Calcite

Elements	Intensity	Contents
Magnesium(Mg)	0.0004	0.5217
Aluminum(Al)	0.0038	1.2314
Silicon(Si)	0.0281	2.7804
Phosphorous(P)	0.0055	0.2573
Sulphur(S)	0.0076	0.5684
Calcium(Ca)	0.6241	61.2238
Titanium(Ti)	0.0001	0
Manganese(Mn)	0.0001	0.0015
Cobalt(Co)	0.0001	0.0007
Iron(Fe)	0.0096	0.9938
Nickel(Ni)	0.0002	0.0089

Elements	Intensity	Contents
Copper(Cu)	0.0006	0.0117
Zinc(Zn)	0.0007	0.022
Gold(Au)	0	0.0272
Silver(Ag)	0.0001	0.0025
Rubidium(Rb)	0.0004	0.0015

[22]

2.4.1. Results of Sieve Analysis of Ikpeshi basalt (test feed) to ball mill

Table 3. Sieve size analysis of Ikpeshi basalt (test feed) to ball mill.

Sieve size (µm)	Sieve size range (µm)	Weight retained (g)	% weight retained retained	Cumulative weight retained (%)	Cumulative weight passing (%)
1000	1000	13.383	13.502	13.502	86.498
-1000+710	710	3.791	3.825	17.327	82.673
-710 + 500	500	4.727	4.769	22.096	77.904
-500 +355	355	4.204	4.241	26.337	73.663
-355+ 250	250	15.772	15.913	42.250	57.750
-250 + 180	180	30.558	30.831	73.081	26.919
-180 + 125	125	0.022	0.022	73.103	26.897
-125 + 90	90	0.088	0.089	73.192	26.808
-90 +63	63	0.198	0.200	73.392	26.608
-63	Pan	26.373	26.608	100.00	0.00
Total		99.116			

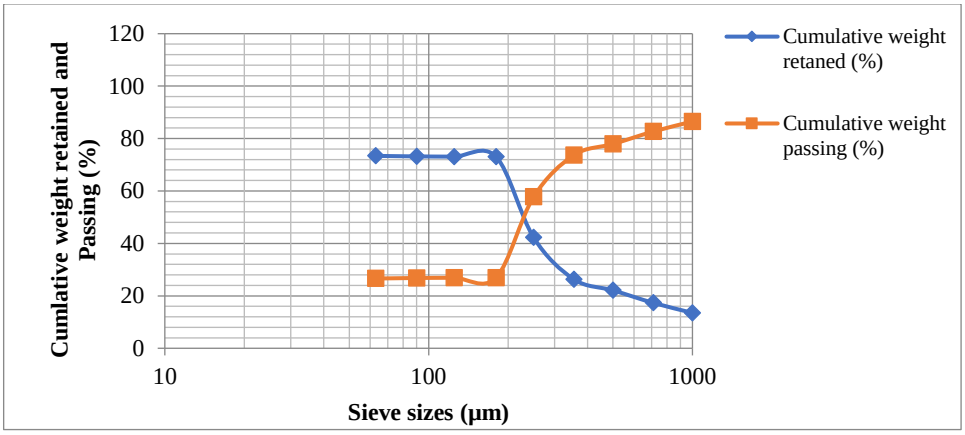

Figure 1. Cumulative weight retained (%) and cumulative weight passing (%) against Sieve size (µm) of Ikpeshi basalt feed to the ball mill

Therefore, from Table 2 and Figure 1, to obtain 80% passing, the size of the sieve will be calculated using the Guadin Schumann expression in Equation (3)

$$X\mu m = \left(\frac{\frac{80}{100}}{\frac{77.904}{100}}\right)^2 = 500 \times = \left(\frac{0.8000}{0.77904}\right)^2 \times 500 =$$

$$(1.026905)^2 \times 500 = 1.054534 \times 500 = 527.27\ \mu m$$

Test feed of Basalt (Ft) = 527.27 µm at 80%.

2.4.2. Sieve size analysis of Ikpeshi basalt (test product) from ball mill

Table 4. Sieve size analysis of Ikpeshi basalt (test product) from ball mill

Sieve size (µm)	Sieve size range (µm)	Weight retained (g)	% weight retained retained	Cumulative weight retained (%)	Cumulative Weight passing (%)
1000	1000	0.970	0.976	0.976	99.024
-1000+710	710	0.336	0.338	1.314	98.686
-710 + 500	500	0.561	0.564	1.878	98.122
-500 +355	355	0.475	0.478	2.356	97.644
-355+ 250	250	2.696	2.712	5.068	94.932
-250 + 180	180	27.815	27.981	33.049	66.951
-180 + 125	125	0.285	0.287	33.336	66.664
-125 + 90	90	0.186	0.187	33.523	66.477
-90 +63	63	0.463	0.466	33.989	66.011
-63	Pan	65.618	66.011	100.00	0.00
Total		99.405			

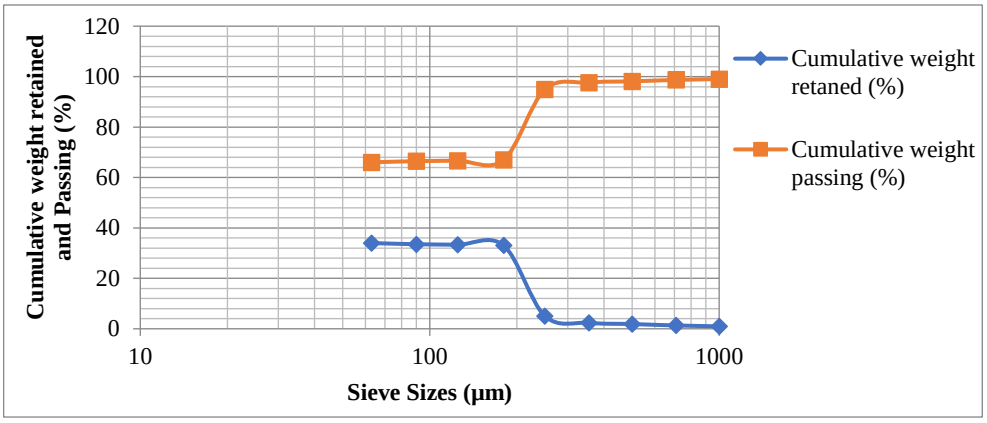

Figure 2. Cumulative weight retained (%) and cumulative weight passing (%) against Sieve size (µm) of Ikpeshi basalt product from the ball mill

Therefore, from Table 3 and Figure 2, to obtain 80% passing, the sieve size will be calculated using the Gaudin Schumann expression in equation (3)

$$X\mu m = \left(\frac{\frac{80}{100}}{\frac{66.951}{100}}\right)^2 \times 180 = \left(\frac{0.8000}{0.66951}\right)^2 \times 180 =$$

$$(1.194904)^2 \times 180 = 1.427796 \times 180 = 257.00\ \mu m$$

Test product (Pt) of the Basalt = 257.00 µm at 80%.

2.4.3. Sieve size analysis of Ikpeshi calcite as reference mineral (test feed) to ball mill

Table 5. Sieve size analysis of Ikpeshi calcite as reference mineral (test feed) to ball mill

Sieve size (µm)	Sieve size range (µm)	Weight retained (g)	% weight retained retained	Cumulative weight retained (%)	Cumulative weight passing (%)
1000	1000	14.346	14.510	14.510	85.490
-1000+710	710	0.390	0.394	14.904	85.096
-710 + 500	500	0.451	0.456	15.360	84.640
-500 +355	355	0.440	0.445	15.805	84.195
-355+ 250	250	1.011	1.023	16.828	83.172
-250 + 180	180	35.979	36.391	53.219	46.781
-180 + 125	125	0.032	0.032	53.251	46.749
-125 + 90	90	0.313	0.317	53.568	46.432
-90 +63	63	0.304	0.308	53.876	46.124
-63	Pan	45.602	46.124	100.00	0.00
Total		98.868			

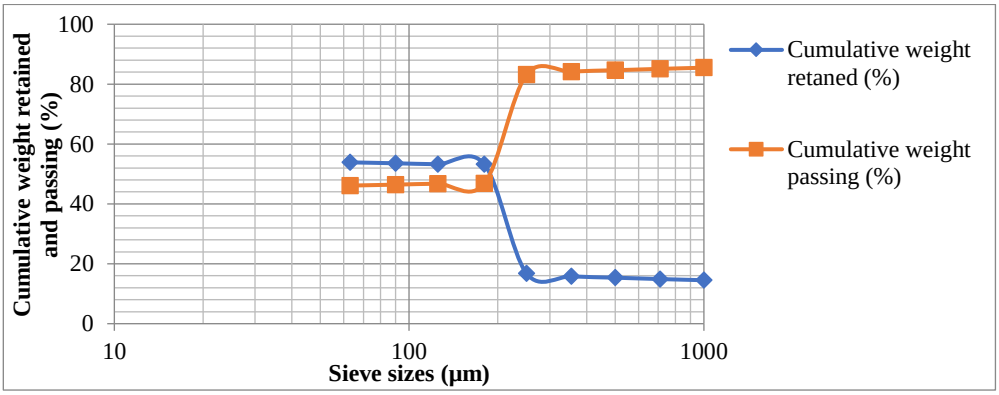

Figure 3. Cumulative weight retained (%) and cumulative weight passing (%) against Sieve size (µm) of Ikpeshi calcite (reference mineral) feed to the ball mill.

Therefore, from Table 4 and Figure 3, to obtain 80% passing, the sieve size will be calculated using the Gaudin Schumann expression in Equation (3)

$$X\mu m = \left(\frac{\frac{80}{100}}{\frac{83.172}{100}}\right)^2 \times 250 = \left(\frac{0.8000}{0.83172}\right)^2 \times 250 =$$

$$(0.961862)^2 \times 250 = 0.925179 \times 250 = 231.29\mu m$$

Test feed of Calcite (Frs) = 231.29 µm at 80%.

2.4.4. Sieve size analysis of Ikpeshi calcite as reference mineral (test product) from ball mill

Table 6. Sieve size analysis of Ikpeshi calcite deposit as reference mineral (test product) from ball mill

Sieve size (µm)	Sieve size range (µm)	Weight retained (g)	% weight retained retained	Cumulative weight retained (%)	Cumulative weight passing (%)
1000	1000	0.575	0.578	0.578	99.422
-1000+710	710	0.087	0.088	0.666	99.334
-710 + 500	500	0.107	0.108	0.774	99.226
-500 +355	355	0.052	0.052	0.826	99.174
-355+ 250	250	0.208	0.209	1.035	98.965
-250 + 180	180	18.976	19.091	20.126	79.874
-180 + 125	125	0.856	0.861	20.987	79.022
-125 + 90	90	0.291	0.293	21.280	78.720
-90 +63	63	0.755	0.760	22.040	77.96
-63	Pan	77.492	77.960	100.00	0.00
Total		99.399			

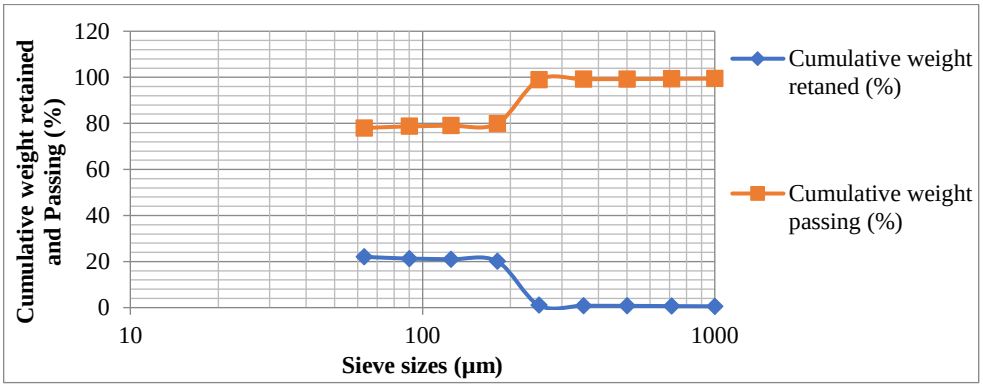

Figure 4. Cumulative weight retained (%) and cumulative weight passing (%) against Sieve size (µm) of Ikpeshi calcite product from the ball mill.

Therefore, from Table 5 and Figure 4, to obtain 80% passing, the sieve size will be calculated using the Gaudin Shumann expression in Equation (3)

$$X\mu m = \left(\frac{\frac{80}{100}}{79.874}\right)^2 \times 180 = \left(\frac{0.8000}{0.79874}\right)^2 \times 180 = (1.001577)^2 \times 180 = 1.003156 \times 180 = 180.57\mu m$$

Test product of Calcite (Prs) = 180.57 μm at 80%

The work index (Wit) of Ikpeshi basalt was determined using equation (4), $Wit = \frac{P}{10\left(\frac{1}{\sqrt{Pt}} - \frac{1}{\sqrt{Ft}}\right)}$

Where P is Net power required = 3.37KWh/t as estimated, Ft = 527.27 μm at 80% passing, Pt = 257.00 μm at 80% passing

Work index of Ikpeshi Basalt (Wit) = $\frac{3.37}{10\left(\frac{1}{\sqrt{257}} - \frac{1}{\sqrt{527.7}}\right)} = \frac{3.37}{10\,(0.062 - 0.044)}$

Work index of Ikpeshi Basalt (Wit) = $\frac{3.37}{10\,(0.018)} = \frac{3.37}{(0.18)}$ = 18.722KWh/t

Therefore, the energy required for comminution of Ikpeshi Basalt to its liberation size is, using equation (6), $Et = Wit\left(\frac{10}{\sqrt{Pt}} - \frac{10}{\sqrt{Ft}}\right)$

$Et = 18.722\left(\frac{10}{\sqrt{257}} - \frac{10}{\sqrt{527.27}}\right) =$

$Et = 18.722\left(\frac{10}{16.0312} - \frac{10}{22.9624}\right) =$

$Et = 18.722(0.6238 - 0.4355) =$

$Et = 18.722 \times 0.1883 = 0.8756 = 3.52KWh$

Therefore, the required energy for comminution of Ikpeshi Basalt to a size suitable for soil amendment is 3.52 KWh.

2.5. Discussion

According to [23], basalt's mineralogy is categorized by the major constituents of calcic-plagioclase feldspar, partially olivine, and augite. With no elutriation or groundwater leaching, basalt is a primordial rock that is abundant in iron, calcium, magnesium, and trace minerals. According to [24], basalt rock dust is healthy for aquatic plants and animals and is not harmful. Plagioclase fieldspar, olivine, pyroxene, amphibole, and albite are the constituents of Ikpeshi basalt rock, according to the laboratory study. The results of X-ray Diffraction procedure on Ikpeshi basalt rock show a greater percentage of silicon oxide (48.32 %), followed by alumiium oxide (13.12%), followed by iron oxide (8.02%), and closely followed by phosphorus oxide, potassium oxide, and calcium oxide with a value range of (7.63, 6.76, and 6.19, respectively). Others include: magnessium oxide (5.05%), tin oxide (1.48%), sodium oxide (1.42%), and value for loss on ignition (1.32%) as shown in Table 1.

The results show that basalt aggregates of Ikpeshi are suitable as mineralizers for agricultural soil because of its high silicate, calcium, magnesium, and potassium contents.

Ikpeshi calcite with a chemical formula of $CaCO_3$, the chemical analysis shows that, the calcium intensity is 0.6241, with content of 61.2238, and other elements as shown in the table 2 above. The chemical analysis shows that the following: Mg, Al, Si, P, S, Ca, Ti, Mn, Co, Fe, Ni, Cu, Zn, Au, Ag, and Rb are the major element of the calcite sample [22].

The results of fractional sieve analysis on the feed to ball mill and product from the ball mill of Ikpeshi basalt samples are shown in Figure 1 and 2, while Figures 3 and 4 show the graph of the particle size analysis of reference ore for 80% passing for both feed and product sieve size fractions for the test basalt and reference ores (calcite). Figure 1 and 2 show that 80% passing was obtained to be 527.27 µm and 257.00 µm for the test feed (Ft) and product (Pt) of the Basalt respectively using equation (3). From Figure 3 and 4 to obtain 80% passing, the test feed (Frs) and product (Prs) sieve size of calcite as reference ore was calculated to be 231.29 µm and 180.57 µm respectively using equation (3).

Work index (Wit) of Ikpeshi basalt as test ore, was calculated to be 18.7222kWh/t with 10.1 kWh/t as work index of calcite as the reference mineral (Wrs) using equation (4), which is in line with international acceptable standard [25]. This led to the calculation of energy used in grinding Ikpeshi basalt to its liberation size to be 3.52 kWh using Equation (6), out of which part of the energy was used for actual grinding while others are converted into other forms such as heat and noise.

These shows that ball milling will effectively reduce the size of Ikpeshi basalt particles and processing Ikpeshi basalt can require more cost and energy for grinding compare to the overburden calcite. The value of the work index suggests advantageous features of the milling processes, which may result in moderate operational cost and improved processing techniques. Finally, the analysis offers important information on energy consumption and milling efficiency of Ikpeshi basalt to economic value for potential adoption as soil mineralizer.

3. Conclusion

The grindability of Ikpeshi basalt was successfully completed to enhance its suitability for soil amendment. The following conclusion was arrived;

(i) The work index of Ikpeshi basalt was calculated to be 18.722 KWh/ton compared to 10.10KWh/ton estimated for calcite.

(ii) The energy required to ground Ikpeshi basalt to its liberation size was calculated to be 3.52 kWh.

(iii) The findings highlight that processes such as crushing and ball milling will effectively reduce the size of Ikpeshi basalt, thereby making them to be more economical for agricultural use.

Acknowledgement. The authors acknowledge Eguje Nigeria Enterprise at Ikpeshi town quarry section, Edo State, Nigeria for assisting with identification and provision of basalt rock sample. Also, the authors are grateful to the department of Mining Engineering, and Agricultural and Bioenvironmental Engineering Technology, Auchi Polytechnic, Auchi, Edo State, Nigeria for providing laboratory assistant for the research.

Authors Contribution. All the authors contributed to formulating, developing, and drafting this research article.

Conflicts of Interest. The authors declare that there exist no known competing interests that could have appeared to influence the work reported in this paper.

References

1. V. Courtillot and J. Ren, On the ages of flood basalt events, *Comptes Rendus Geoscience*, 335(1), 2003, pp. 113–140.
2. N. H. Sleep, Evolution of the continental lithosphere, *Annual Review of Earth and Planetary Sciences*, 33, 2005, pp. 369–393.
3. A. D. Saunders, Large igneous provinces: Origin and environmental consequences, *Elements*, 1(5), 2005, pp. 259–263.
4. L. Baker, J. Smith, R. Jones, Nutrient release from basalt rock dust and its effects on soil fertility, *Agricultural Sciences*, 3(4), 2012, pp. 521–529.
5. J. L. Havlin, J. D. Beaton, S. L. Tisdale, W. L. Nelson, *Soil Fertility and Fertilizers: An Introduction to Nutrient Management*, Pearson Prentice Hall, 2014.
6. R. R. Van der Ploeg, W. de Vries, L. Kooistra, Soil quality and agricultural productivity in the tropics: A review, *Soil Use and Management*, 29(3), 2013, pp. 300–314.
7. R. O. Miller, S. Kuo, W. L. Hargrove, Micronutrient availability in soils amended with basalt, *Soil Science Society of America Journal*, 80(5), 2016, pp. 1078–1087.
8. J. M. Tisdall, J. M. Oades and P. G. Saffigna, The role of soil amendments in improving soil fertility, *Agriculture, Ecosystems and Environment*, 202, 2014, pp. 1–10.
9. A. L. Lewis, B. Sarkar, P. Wade, S. J. Kemp, M. E. Hodson, L. L. Taylor, C. Taylor, J. Quirk, D. J. Beerling, Effects of mineralogy, chemistry and physical properties of basalts on carbon capture potential and plant-nutrient element release via enhanced weathering, *Applied Geochemistry*, 132, 2021, pp. 105023.

10. J. Bennett, P. Smith, M. Taylor, The role of mineralogy in soil amendment effectiveness, *Soil Science Society of America Journal*, 79(4), 2015, pp. 1234–1245.
11. M. Dumont, C. Legrand, G. Morin, Zeolite-rich basalt: A potential resource for soil amendment, *Geological Society of America Bulletin*, 130(1–2), 2018, pp. 217–229.
12. A. Bhandari, R. Gupta, S. Kumar, Grindability of rocks: A review, *International Journal of Mining Science and Technology*, 30(5), 2020, pp. 581–590.
13. F. C. Bond, Crushing and grinding calculations, *British Chemical Engineering*, 6(6), 1961, pp. 378–385.
14. M. Harris, T. Johnson, D. Lee, Influence of mineral composition on the grindability of basalt, *Minerals Engineering*, 171, 2021, pp. 107–115.
15. A. Hernández, J. Pérez, A. Rodríguez, Empirical models for predicting grindability of geological materials, *Journal of Mining Science*, 56(1), 2020, pp. 145–154.
16. A. Kumar, R. Singh, P. Verma, Digital imaging techniques for particle size analysis in mineral processing, *Mineral Processing and Extractive Metallurgy Review*, 43(3), 2022, pp. 235–248.
17. J. Fitzgerald, A. Jones, L. Smith, Environmental impacts of basalt mining: A case study, *Environmental Impact Assessment Review*, 73, 2018, pp. 1–10.
18. J. Lehmann, S. Joseph, *Biochar for Environmental Management: Science, Technology and Implementation*, Routledge, 2015.
19. M. Müller, H. Schneider, J. Becker, Economic analysis of soil amendments: Comparing basalt and other materials, *Agricultural Economics*, 51(3), 2020, pp. 345–357.
20. O. R. Ehidiamen, J. I. Ehilenboadiaye, C. I. Omoigiade, Tomographical evaluation of subsurface mineral composition in Ozalla, Edo State Nigeria, *Journal of Applied Science and Environmental Management*, 23(4), 2019, pp. 617–620.
21. O. O. Alabi, O. W. Awogbamila, Determination of grindability characteristics of Duguri (Nigeria) galena towards effective beneficiation process, *Science and Technology*, 6(22), 2020, pp. 83–92.
22. S. Adakole, S. O. Osaghae, E. B. Sanni, M. M. Mohammed, Quality assessment of Ikpeshi white calcite deposit, *Advanced Journal of Science, Technology and Engineering*, 3(1), 2023, pp. 75–83.
23. I. Al-Akhaly, Engineering properties of basalt coarse aggregates in Hamdan area, north west Sana'a, Yemen, *Journal of Geological Engineering*, 42, 2018, pp. 159–174.

24. M. Al-Rawashdeh, A. Shaqadan, Effect of basalt aggregates and plasticizer on the compressive strength of concrete, *International Journal of Engineering and Technology*, 4(4), 2015, pp. 520–525.
25. N. L. Weiss, Particle characterization, *Mineral Processing Handbook,* American Institute of Mining and Metallurgical, 1985, pp. 142–156.

Addresses:

- Engr. Rasheed Ibrahim (Department of Agricultural and BioEnvironmental Engineering Technology, School of Engineering Technology, Auchi Polytechnic, Auchi, Edo State, Nigeria)
  ibbrroo88@gmail.com
  (**corresponding author*)
- Prof. Akinbile Oluwakunmi Christopher (Department of Agricultural and Environmental Engineering, School of Infrastructure, Minerals and Manufacturing Engineering, Federal University of Technology, Akure)
  coakinbile@futa.edu.ng
- Prof. Babatunde Sunday Ewulo (Department of Crop, Soil and Pest Management, School of Agriculture and Agricultural Technology, Federal University of Technology, Akure).
  bsewulo@futa.edu.ng
- Prof. Ayodele Olumuyiwa Owolabi (Department of Mining Engineering, School of Infrastructure, Minerals and Manufacturing Engineering, Federal University of Technology, Akure).
  aoowolabi@futa.edu.ng
- Engr. Sunday Adakole (Department of Mineral and Petroleum Resources Engineering Technology, School of Engineering Technology, Auchi Polytechnic, Auchi, Edo State Nigeria).
  adakolesunnymaxfur@gmail.com
- Engr. Asishana Stanley Ajayi (Department of Agricultural and BioEnvironmental Engineering Technology, School of Engineering Technology, Auchi Polytechnic, Auchi, Edo State, Nigeria)
  ajayistan@gmail.com

STUDIA UNIVERSITATIS BABEŞ-BOLYAI
Engineering 70(1) 2025 DOI: 10.24193/subbeng.2025.6

Review on the Integration of Biochar and Internet of Things (IoT) for Atmospheric Carbon Sequestration

Abdul Rasheed Ibrahim*, Adeboye John Arohunmalase,
Alexander Oluwasegun Adepetoye, Ogbonna Gospel Nwokocha

Abstract. *The continuous increase in atmospheric carbon dioxide is a major factor affecting climate change. Biochar, a product realized from pyrolysis of biomass feed with abundant carbon, has gained researchers' interests for long-term mitigation of greenhouse gases and sequestration of atmospheric carbon. This study reviews recent literature on the properties, production, and biochar's potential in the sequestration of atmospheric carbon. It was reviewed that the application of biochar from rice husk, corn stover, sugarcane bagasse, sawdust, and animal manure to the field at the rates of 10, 12, 15, 8, and 10t/ha, will reduce the emission of greenhouse gases by 20, 50, 40, 18, and 55%, respectively. The current trends of incorporating IoT for the monitoring of real-time soil and climate carbon dynamics were also investigated. The review revealed that the adoption of biochar and IoT technologies provides sustainable, scalable, and transparent approaches to sequestration of atmospheric carbon.*

Keywords: *Biochar, Biomass, Carbon sequestration, Greenhouse Gas.*

1. Introduction

The global environment is faced with climate change problems, affecting ecosystems, livelihoods of humans, and weather patterns. The excess release of atmospheric CO_2 is one of the major contributors to the release of atmospheric greenhouse gases and climate change effects [1]. The emission of these gases is majorly a result of anthropogenic activities, such as combustion of fossil fuel and deforestation [2]. The effects have been serious, with a significant increase in the level of atmospheric CO_2, which has led to global temperature escalation [1]. In 2020, the concentration of world atmospheric

CO_2 peaked at 412 parts per million. If rapid steps to reduce these emissions are not developed and implemented by the year 2030, the concentration of atmospheric CO_2 could increase to alarming levels of 600 to 1500 [3].

The loss of a large amount of soil carbon has been attributed to an increase in atmospheric CO_2 levels [4], posing a serious challenge to the quality and yield of crops [5]. This concern arises due to an increase in population which will lead to increase in the demand for food in the coming years [6]. Moreover, the health consequences of prolonged and frequent exposure to atmospheric CO_2 beyond 1000 ppm were highlighted by recent studies [7]. The impacts of these consequences include reduction in bone mineral density, inflammation, formation of carbon deposits in the kidney, compromised higher-level cognitive functions, impaired endothelial function, and increased oxidative stress [7]. Due to these challenges, it becomes crucial to implement and explore techniques that effectively reduce emission of carbon to reduce atmospheric CO_2 and facilitate long-term sequestration of soil carbon to retain carbon that is stable in the soil. Taking measures that are decisive is crucial to address the negative effects of climate change and secure a future that is sustainable for both the well-being of humans and the natural environment.

Biochar is a solid material that is derived from biomass mainly through a process that is thermochemical under high-temperature and pressure conditions in the absence of oxygen. Recently, biochar was reported as a promising soil mineralizer due to its interaction with soil systems and physicochemical properties that are unique [8]. When added to soils, biochar improves the fertility of the soil, soil water holding capacity, and nutrient retention. Its porous attributes provide a home for microorganisms that are beneficial, promoting the growth of plants, and improving soil health [9]. Furthermore, biochar has high microbial stability and chemical attributes due to its remarkable molecular structure. A significant long-term study conducted over an eight year's period evaluated biochar's decomposition from ryegrass using ^{14}C compound analysis. The study revealed a slow decomposition rate that is exceptional, with the biochar losing only a carbon content of $7\times10-4\%$ per day under ideal conditions [10]. This signifies that for biochar to lose 1% of its carbon content, it would take nearly 400 years. In another study, the residence time of biochar derived from *Eucalyptus saligna*, pyrolyzed, was assessed at 550°C and subsequently added to soils at 20°C. The study reported remarkable long-term residence time for biochar, with an average residence time range from 732 to 1061 years [11]. These studies validated and established the compelling evidence about the enduring nature of biochar as an effective carbon sink, emphasizing its role as a long-lasting and sustainable solution and alternative for the sequestration of soil carbon.

Despite the potential of biochar gaining researchers' interests for improving soil carbon storage and mitigating climate change effects [12], there is a need to balance the identification of research priorities and the existing knowledge, and fill the understanding

gaps. The objective of this review is to connect the bridge of these knowledge gaps by analyzing the mechanisms, properties, and incorporation of IoT associated with the application of biochar for the sequestration of atmospheric and soil carbon. Despite the potential of biochar to reduce the accumulation of atmospheric carbon dioxide (CO_2) by improving biomass yields, a recent and comprehensive overview of its properties will assist in making decisions, support the establishment of standardized protocols, and guide future research in this field of study. Majorly, the collaborative effort on the adoption and use of biochar for atmospheric carbon sequestration will pave the way for the global fight against climate change. Also, this review considers various fields and guidelines for biochar production as well as the present state of industries in the business of atmospheric carbon removal, it provides guidelines that can assist in the design and development of a commercial biochar production system tailored towards removal of atmospheric carbon. The investigation will cover the techniques involved in the analysis of common feedstock, technologies of production.

2. Production and Characteristics of Biochar

The effectiveness and properties of biochar are connected to the processes and materials used in its production [13]. A proper comprehension of the pyrolysis techniques and feedstocks is crucial to the use of biochar for specific environmental and agricultural applications. The variability in its condition of pyrolysis and nature of raw biomass produces biochars with unique physicochemical properties that determine their potential for sequestration of atmospheric carbon, behavior in soil, and suitability for various uses in agronomic studies.

2.1 Biomass Feedstocks

Biochar can be produced from different feedstocks, broadly categorized into animal manure, forestry by-products, agricultural residues, and municipal organic wastes. The critical determinant for chemical composition, porosity, ash content, elemental ratios (C: N, C: O), and specific surface area of the final biochar product is feed biomass. The residues from agriculture, such as wheat straw, coconut shells, rice husks, sugar bagasse, and corn stover are among the most commonly utilized feedstocks due to their renewable nature, high lingo cellulosic content, and abundance. These residues produce biochars with high carbon contents and low ash, and this favor soil carbon stability for long periods. Wastes from forestry, such as bark, sawdust, wood chips, and tree trimmings, offer a biomass source that is rich in lignin. Biochars produced from materials that are woody generally exhibit structural rigidity, aromaticity, and high surface stability, making them suitable for sequestration of carbon. Manures from animal source such as swine manure, poultry litter, and cow dung, though with reduced carbon abundance, are unique for producing biochars that is nutrient-enriched. These

feedstocks produced biochars with high quantities of potassium, phosphorus, and other micronutrients, making them suitable for soil amendments but less suitable for carbon storage for long period due to lower stability of carbon and higher content of ash. Green waste from municipals, such as kitchen scraps, yard trimmings, and compostable urban biomass, is another feedstock that is viable while offering management of organic waste, these resources often exhibit composition that is heterogeneous, necessitating feedstock homogenization and pre-treatment for the quality of the biochar to be consistent.

2.2 Pyrolysis Process

The thermochemical decomposition of organic matter in an anaerobic environment is called pyrolysis, leading to the production of biochar (solid), bio-oil (liquid), and non-condensable (syngas). The properties and distribution of these products are significantly affected by pyrolysis type and procedure employed, which are largely defined by heating rate, temperature, and residence time.

2.2.1 Slow pyrolysis

The maximization of biochar yield is commonly achieved by this method. It is usually carried out at a moderate range of temperature from 300°C to 500°C with extended residence time, the process of slow pyrolysis favors the formation of biochar that is stabilized and rich in carbon. The steady volatilization of organic compounds is achieved by prolonged exposure to heat, producing biochar with improved porosity, aromaticity, and a higher carbonization degree.

2.2.2 Fast pyrolysis

This process occurs at a similar temperature range that is relative to the slow pyrolysis process (350°C–600°C) but involves fast rates of heating and short vapor residence times (seconds). The process of fast pyrolysis is primarily designed for bio-oil production, with the secondary product being biochar. Greater heterogeneity and lower stability in terms of composition and structure are the results of biochar produced with the fast pyrolysis method [14].

2.2.3 Gasification

The process of gasification involves heating of biomass at a higher temperature range often greater than 700°C, under limited and controlled aerobic conditions or the introduction of steam to oxidize the biomass partially. The aim of gasification of biomass is to produce syngas (a mixture of CH4, CO, H_2), the end product, which is biochar, is usually produced in reduced quantities and may have unique physicochemical properties, such as reduced surface functionality and high ash content (15;16].

2.3 Review and Benefits of Different Biochar Sources for Climate Mitigation

Table 1 reveals the conversion of biomass from different feedstocks' sources to biochar, and this has prevailed as a promising approach and amendment for greenhouse gas emission reduction from agricultural soils. The table reveals and compares the effectiveness of five types of biochar, such as rice husk, corn stover, sugarcane bagasse, sawdust, and animal manure in reducing emissions of carbon dioxide (CO_2), methane (CH_4), and nitrous oxide (N_2O) from different types of soil at varying application rates.

2.3.1 Greenhouse Gas Mitigation Potential

Table 1 reveals that different biochar reduces the emission of greenhouse gases differently, the biochar produced from animal manure generated the highest methane (CH_4) reduction potential, achieving a reduction potential of 55% when applied at the rate of 10t/ha.. Similarly, biochar derived from corn stover demonstrated improved efficacy in the mitigation of methane, reducing methane emissions by 50% at the application rate of 12t/ha on sandy soils. These results signify that organic residues produced biochars with high lignin and nutrient content that are majorly effective for the reduction of methane in a soil that is well-drained.

Also, biochar produced from sugarcane bagasse reduced nitrogen oxide (N_2O) emissions by 40% when applied to clay soil at the rate of 15 t/ha. The capacity to retain ammonium and its increased surface area determine the effectiveness of biochar in mitigating the emission of nitrous oxide (N_2O), especially greenhouse gas that is potent, thereby preventing nitrification and denitrification processes in soils that are heavier in nature.

Table 1 also reveal moderate reductions of about 20% and 18% for mitigating carbon dioxide (CO_2) emissions when rice husk and sawdust biochars are used, respectively. A comparable mitigation of carbon dioxide (CO_2) emission was achieved when biochar from rice husk was applied at the rate of 10t/ha to loamy soil and biochar from sawdust was applied at the lower rate of 8t/ha to sandy loam soil. Though, the performance of biochar produced from woody and cellulose-rich biomass for mitigating greenhouse gas emission appear to be low compared to biochars meant for reducing methane and nitrous oxide, their potential for improving soil carbon retention was highlighted in this result.

2.3.2 Soil Type and Application Rate Considerations

The texture of soil determines the effectiveness of biochar application. Loamy soil was reported to have the highest mitigation potential for both methane (CH_4) and carbon IV oxide (CO_2) emissions, whereas the mitigation of nitrogen oxide (N_2O) was better in clay soil. Despite low nutrient and moisture retention of sandy soil,

biochar from corn stover mitigates methane emission effectively in sandy soils, suggesting a possible relationship between soil drainage properties and biochar porosity.

2.3.3 Application Rates

The reduction of greenhouse gas emissions also depends on the application rates of biochar. The higher the application rate of biochar, the higher the reduction in greenhouse gas emission, as reported in Table 1 for corn stover and sugarcane bagasse at application rates of 12 and 15t/ha, respectively. However, this trend was not completely linear, as biochar from animal manure demonstrated the highest mitigation for methane (CH_4) at a moderate application rate of 10 t/ha, this signifies that biochar source and properties may affect its application dosage for reducing greenhouse gas emission in some cases.

Table 1. Biochar's Role in Reducing Greenhouse Gas Emissions from Soil

Biochar Type	Greenhouse Gas	Reduction Emission (%)	Soil Type	Application Rates (t/ha)
Rice husk	CO_2	20	Loamy soil	10
Cornstover	CH_4	50	Sandy soil	12
Sugarcane bargass	N_2O	40	Clay soil	15
Saw dust	CO_2	18	Sandy Loam	8
Animal manure	CH_4	55	Loamy Soil	10

[14]

2.4 Process of Atmospheric Carbon Sequestration by Biochar

The three major techniques for improving climate change effects are negative emissions, conventional emissions, and radioactive. The reduction of emission, nuclear power, fuel switching, efficiency gains, storage technologies, and carbon capture through a renewable energy approach is the focus of conventional emission. The methods for removing atmospheric carbon, such as technological, biogenic, and hybrid carbon sequestration approaches, are the new methods also referred to as negative emissions. This involves soil carbon sequestration, direct air carbon capture and storage, bio-carbon capture and storage by bioenergy, wetland restoration, forestation, biochar, ocean fertilization, enhanced terrestrial weathering, biomass utilization, alkalinity enhancement, and mineral carbonization.

The development of financially and effectively carbon removal projects is crucial due to the present state of emergency in climate issues. Biochar improves atmospheric carbon capturing, utilization, and storage, it has been considered as a negative emissions technology that is promising [17]. The process of photosynthesis that occurs during plant growth assists in achieving the removal of atmospheric carbon

coupled with a conversion process that is thermochemical and results in the formation of a solid carbonaceous material called biochar. Biochar possesses a carbon formation that is very stable and can withstand biological and thermal degradation for a long period of time. The biochar can then be mixed and stored in soils, building various carbon sinks and structures, where its additional benefits can be derived. It is projected that atmospheric carbon removal in the range of 0.3–2 Gt CO_2 $year^{-1}$ through biochar application will be achieved by 2050 [18].

The potential of carbon sequestration by biochar is remarkably affected by its surface area and particle size. Smaller particle sizes (diameter of less than 0.045 mm) and larger surface areas (exceeding 100 m^2/g) offer benefits that are numerous. Initially, the reduction of biochar particle size improves the area of contact between the surrounding environment and biochar, improving the interaction and adsorption of greenhouse gas emissions such as CH_4, CO_2, and N_2O [9]. This increase in surface contact allows for more effective retention and capture of carbon within the biochar structure. A Recent study conducted on biochar produced from different-sized fruit shells of *Camellia oleifera* revealed that the smallest fruit shell sizes, ranging from 0.5 to 2 mm were attributed to the lowest emission rates of CO_2 and N_2O [19]. Larger fruit shell sizes ranging from 2–5 mm or 5–10 mm generally have a surface area-to-volume ratio that is lower, which restricts accessibility to microbes and subsequent degradation. Therefore, biochar particles that are large may exhibit CO_2 efflux reduction due to reduction in the activity of microbes and slower rates of decomposition.

2.5 The Role of IoT for Monitoring Environmental Hazards

As a result of different changes experienced in the environment, the sharing of data and its reuse with the assistance of artificial intelligence instruments and algorithms, play a crucial role in assisting researchers to protect the environment that is continuously threatened and ensure the development of environmental management practices that are sustainable. Scientists can utilize online data platforms and sharing tools that consist intricate and vast environmental and earth science data like, climatic and atmospheric data, hydrology, pedology, ecology, and biodiversity [20] for theories testing, analysis, and interpretation, model prediction and experimental data that lead to better understanding of the environment.

The use of artificial neural networks (ANN) for short- and long-term forecasting applications for air pollution has been adopted. An environmental toxicology model enabled by IoT to detect air pollution was developed [21]. A model was developed to report real-time monitoring of air quality using artificial intelligence with the adoption of a broadcast alarm and cloud server when hazardous pollutants are detected in the air. The artificial algae algorithm (AAA) and Elman neural network (ENN) models predict and classify air quality in future timestamps. The data collected by sensors are sent to a cloud server with the aid of WiFi gateways. The artificial algae

algorithm (AAA) model optimizes the Elman neural network (ENN) model parameters during data processing.

The popularity of unmanned machines and artificial intelligence arises from the real-time and effective automated solutions that these technologies provide when placed in toxic environments. They can discover and isolate potential threats before they cause harm, with reduced or no human involvement [22]. Recent technologies have been developed for the integration of robots that are autonomous with flexible sensors and remotely deployed in toxic and unsafe environments. They can improve neighborhood and workers' safety without any threat to human life. These devices are integrated with systems capable of monitoring, exploring, detecting, and alarming when events that are hazardous occur [23].

2.6 Role of Internet of Things (IoT) for Atmospheric Carbon Sequestration

i. Real-time data collection.
   Internet of things devices, such as soil sensors measure parameters like the levels of soil moisture, soil temperature, and soil organic carbon in real-time. These parameters are crucial for the assessment of the efficiency of carbon sequestration.
ii. Remote Monitoring
   Systems that are enabled with IoT provide carbon data that can be remotely accessed, thereby reducing frequent visitation to the field. This is particularly recommended for commercial agroecosystems where manual monitoring is practically impossible.
iii. Integration with GIS and Remote Sensing
   This involves integration of IoT with remote sensing technologies and Geographic Information Systems (GIS) to provide temporal and spatial analyses of carbon sequestration across different agroecosystems.
iv. Data-Driven Decision Making
v. IoT systems enable the analysis of data through machine learning and artificial intelligence algorithms. These approaches assist in the optimization of farm activities, such as cover cropping and crop rotation to maximize the rate of atmospheric carbon sequestration.

2.7 Applications of IoT in Carbon Sequestration

i. Precision Agriculture IoT assists in the accurate monitoring of carbon levels in different farm zones, allowing management that is site specific to improve sequestration of carbon.
ii. Agroforestry Systems IoT tools assist in the monitoring of carbon stocks in the systems of agroforestry by measuring the level of soil carbon, biomass growth, environmental conditions and promoting land-use practices that are sustainable.

iii. Conservation Tillage Sensors are used to monitor disturbance in soil disturbance and level of organic matter under tillage systems that are conservative, thereby optimizing tillage practices for maximum carbon retention.

iv. Carbon Credit Certification IoT provides verifiable and accurate data for the market associated with carbon credits, enabling farmers to make money from their efforts on carbon sequestration. This generates sustainable practices that are incentivized.

2.8 Future Prospects

i. Integration with Artificial Intelligence. Analytics that are artificial intelligence driven will improve applications of IoT by predicting the trend of carbon sequestration and suggesting practices that are adaptive in management.

ii. Blockchain for Carbon Credit Verification. The technology attributed to blockchain can ensure trust and transparency in carbon credit markets by recording carbon data generated from IoT.

iii. Advanced Sensors. The development of sensors with high precision and low cost will make IoT systems more efficient for proper carbon monitoring.

iv. Policy Support Governments and organizations. There is a need to support the adoption of IoT through training, subsidies, and development of infrastructure to scale the efforts on carbon sequestration. [24]

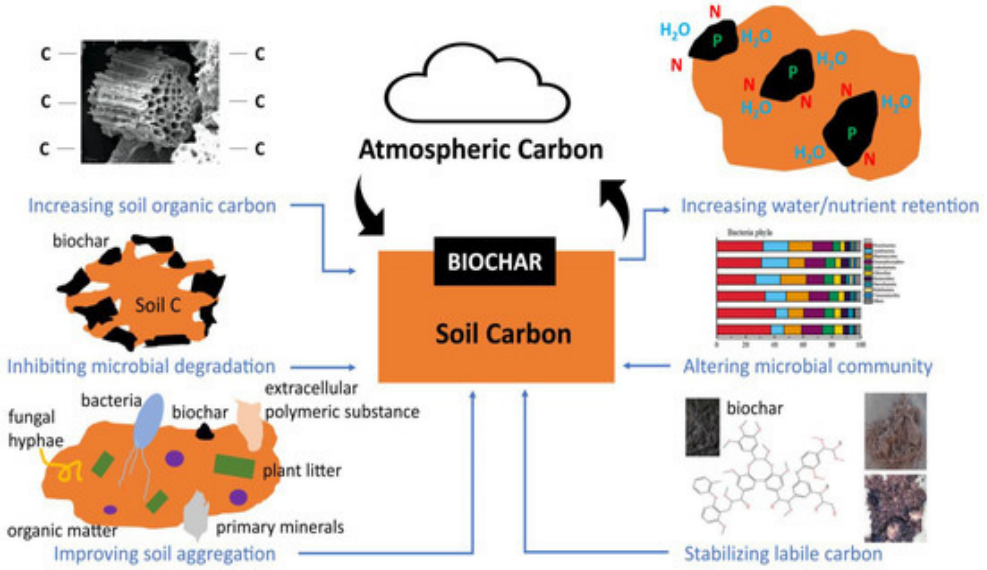

[25]

Fig. 1. Climate benefits of biochar for atmospheric CO_2 removal

3. Conclusion

The monitoring of carbon sequestration through integration with IoT offers an approach that is promising for sustainable agricultural systems and climate change mitigation. By setting up real-time data collection, analysis, and decision-making, IoT technologies improve the effectiveness and efficiency of carbon management practices. However, addressing attributed challenges such as high costs and connectivity issues is crucial to exploring and deriving the full potential of IoT in carbon sequestration.

Acknowledgement. The authors acknowledge Weppa Leventis Farm Agenebode, Edo State, Nigeria, for providing biochar for feasibility study and as a guide for proper review of this study.

Authors Contribution. All the authors contributed significantly to this study.

Conflicts of Interest. The authors declare no conflict of interest that may be attributed to any contents of this study.

References

[1] K. O. Yoro, M. O. Daramola, CO2 emission sources, greenhouse gases, and the global warming effect, in Advances in Carbon Capture, Elsevier, Amsterdam, The Netherlands, 2020, pp. 3–28.

[2] A. M. Driga, A. S. Drigas, Climate Change 101: How Everyday Activities Contribute to the Ever-Growing Issue, *Int. J. Recent Contrib. Eng. Sci. IT*, 7, 2019, 22–31.

[3] M. Mahato, S. Nam, R. Tabassian, S. Oh, V. H. Nguyen, I.-K. Oh, Electronically Conjugated Multifunctional Covalent Triazine Framework for Unprecedented CO2 Selectivity and High-Power Flexible Supercapacitor, *Adv. Funct. Mater*. 32, 2022, 2107442.

[4] J. Chen, L. Elsgaard, K. J. van Groenigen, J. E. Olesen, Z. Liang, Y. Jiang, P. E. Lærke, Y. Zhang, Y. Luo, B. A. Hungate, Soil carbon loss with warming: New evidence from carbon-degrading enzymes, *Glob. Change Biol.*, 26, 2020, 1944–1952.

[5] W. Sun, J. G. Canadell, L. Yu, L. Yu, W. Zhang, P. Smith, T. Fischer, Y. Huang, Climate drives global soil carbon sequestration and crop yield changes under conservation agriculture, *Glob. Change Biol.*, 26, 2020, 3325–3335.

[6] M. van Dijk, T. Morley, M. L. Rau, Y. Saghai, A meta-analysis of projected global food demand and population at risk of hunger for the period 2010–2050, *Nat. Food*, 2, 2021, 494–501.

[7] T. A. Jacobson, J. S. Kler, M. T. Hernke, R. K. Braun, K. C. Meyer, W. E. Funk, Direct human health risks of increased atmospheric carbon dioxide, *Nat. Sustain.*, 2, 2019, 691–701.
[8] J. K. M. Chagas, C. C. de Figueiredo, M. L. G. Ramos, Biochar increases soil carbon pools: Evidence from a global meta-analysis, *J. Environ. Manag.*, 305, 2022, 114403.
[9] W. Liao, S. C. Thomas, Biochar particle size and post-pyrolysis mechanical processing affect soil pH, water retention capacity, and plant performance, *Soil Syst.*, 3, 2019, 14.
[10] Y. Kuzyakov, I. Bogomolova, B. Glaser, Biochar stability in soil: Decomposition during eight years and transformation as assessed by compound-specific 14C analysis, *Soil Biol. Biochem.*, 70, 2014, 229–236.
[11] Y. Fang, B. Singh, B. P. Singh, Effect of temperature on biochar priming effects and its stability in soils, *Soil Biol. Biochem.*, 80, 2015, 136–145.
[12] S. Li, S. Skelly, Physicochemical properties and applications of biochars derived from municipal solid waste: A review, *Environ. Adv.*, 13, 2023, 100395.
[13] K. Qian, A. Kumar, H. Zhang, D. Bellmer, R. Huhnke, Recent advances in utilization of biochar, *Renewable Sustain. Energy Rev.*, 42, 2015, 1055–1064.
[14] B. Bera, Biomass-Derived Biochar and Its Role in Carbon Sequestration and Soil Health Improvement, *Plant Science Review*, 2024.
[15] M. Gupta, N. Savla, C. Pandit, S. Pandit, P. K. Gupta, M. Pant, V. K. Thakur, Use of biomass derived biochar in wastewater treatment and power production: A promising solution for a sustainable environment, *Sci. Total Environ.*, 825, 2022, 153892.
[16] O. A. Wani, F. Akhter, S. S. Kumar, S. Babu, R. H. Kanth, S. A. Mir, S. S. Rathore, Mitigating soil erosion through biomass-derived biochar: exploring the influence of feedstock types and pyrolysis temperature, *Land*, 12(12), 2023, 2111.
[17] A. I. Osman, C. Farrell, A. H. Al-Muhtaseb, A. S. Al-Fatesh, J. Harrison, D. W. Rooney, Pyrolysis kinetic modelling of abundant plastic waste (PET) and in-situ emission monitoring, *Environ. Sci. Europe*, 32(1), 2020, 112.
[18] S. Fawzy, A. O. I. Osman, J. Doran, D. W. Rooney, Strategies for mitigation of climate change: A review, *Environ. Chem. Lett.*, 18(6), 2020, 2069–2094.
[19] Z. H. Weng, X. Liu, S. Eldridge, H. Wang, T. Rose, M. Rose, J. Rust, B. P. Singh, E. Tavakkoli, C. Tang, Priming of soil organic carbon induced by sugarcane residues and its biochar control the source of nitrogen for plant uptake: A dual 13C and 15N isotope three-source-partitioning study, *Soil Biol. Biochem.*, 146, 2020, 107792.

[20] A. M. Basel, K. T. Nguyen, E. Arnaud, A. C. Craparo, The foundations of big data sharing: a CGIAR international research organization perspective, *Front. Environ. Sci.*, 11, 2023, 1107393.
[21] P. Asha, L. Natrayan, B. Geetha, J. R. Beulah, R. Sumathy, G. Varalakshmi, S. Neelakandan, IoT enabled environmental toxicology for air pollution monitoring using AI techniques, *Environ. Res.*, 205, 2022, 112574.
[22] J. Jiang, C. Lin, G. Han, A. M. Abu-Mahfouz, S. B. H. Shah, M. Martínez-García, How AI-enabled SDN technologies improve the security and functionality of industrial IoT network: architectures, enabling technologies, and opportunities, *Digital Commun. Netw*., 9, 2022, 1351–1362.
[23] A. Maedche, C. Legner, A. Benlian, B. Berger, H. Gimpel, T. Hess, et al., AI-based digital assistants: opportunities, threats, and research perspectives, *Bus. Inf. Syst. Eng.*, 61, 2019, 535–544.
[24] G. M. Imran, S. K. Banoth, K. Aruna, B. Lakshman, IoT based carbon sequestration monitoring in agroecosystems, in P. T. Bhaisare (Ed.), Smart Farming: Trends and Innovations in Agriculture & Allied Science, Essay Publication Research and Consultancy, 2025, pp. 79–82.
[25] S. Li, D. Tasnady, Biochar for Soil Carbon Sequestration: Current Knowledge, Mechanisms, and Future Perspectives, C, 9, 2023, 67.

Addresses:

- Ibrahim Abdul Rasheed (Department of Agricultural and Environmental Engineering, School of Infrastructure, Minerals and Manufacturing Engineering, Federal University of Technology, Akure)
  farmpoweroption@gmail.com
  (*corresponding author)
- Arohunmolase Adeboye John (Department of Mineral and Petroleum Resources Engineering, Technology, Auchi Polytechnic, Auchi, Edo State Nigeria)
  arohunmolaseadeboye@auchipoly.edu.ng
- Adepetoye Alexander Oluwasegun (Department of Petroleum and Gas Processing Engineering Technology, Auchi Polytechnic, Auchi, Edo State, Nigeria).
  adepetoye@auchipoly.edu.ng
- Nwokocha Ogbonna Gospel (Department of Electrical Engineering Technology, Auchi Polytechnic, Auchi, Edo State, Nigeria).
  ngospel01@gmail.com

STUDIA UNIVERSITATIS BABEŞ-BOLYAI
Engineering 70(1) 2025 DOI: 10.24193/subbeng.2025.7

A Review of Kinetic Energy Dissipation Systems in Automotive Crashes

Fabrice Chatue, Gilbert-Rainer Gillich*, Zeno-Iosif Praisach, Cristian Tufisi, Zoltan-Iosif Korka

Abstract. *This paper provides an overview of kinetic energy management in road safety. The various elements considered by engineers are analyzed to understand how and why the absorption of kinetic energy generated by a moving vehicle has become a major road safety issue. We examine the corrective measures designed by automotive engineers, which fall into two categories: internal vehicle measures, such as airbags, seat belts, and headrests; and external protective measures, including guardrails and impact attenuators. Impact analysis quantifies the sliding of the guardrails along the rails after an impact, thus absorbing the kinetic energy generated by the vehicle. The results indicate that progressive deformation and adjusted stiffness gradients increase impulse duration and reduce peak deceleration. The dampers primarily manage kinetic energy by redirecting it, with limited energy absorption. Design implications include optimizing post spacing and anchoring rails to the ground to guide the system's pads as they slide backward upon impact.*

Keywords: *road safety, guardrail, kinetic energy, passenger protection systems.*

1. Introduction

The design of road safety devices that dissipate vehicle kinetic energy is essential for reducing risks to occupants, as crash test frameworks [1,2] evaluate performance based on impact severity, redirection, and permissible deformation. Energy dissipation lengthens the impact duration and reduces maximum decelerations, as measured by the EN1317 (ASI/THIV) indices [3].

Analyses show that greater system flexibility (e.g., a larger working width (W)) is correlated with a lower ASI/THIV index [4]. Deformation systems with S235 JR and S355 JR steel posts, combined with W-shaped rails, convert kinetic energy through deformation; therefore, post spacing is crucial to system rigidity. Rail height, along with consideration of post-soil interaction, optimizes energy absorption and controls deflection. It should be noted that, in accordance with EN1317, each crash attenuator installed upstream of a guardrail must include a transition element [5]. Impact resistance assessment programs also emphasize energy-absorbing devices that deform or fold the rail to prevent punctures and slow deceleration. Finally, it is important to emphasize that crash attenuators are essential when obstacles are present. At tunnel entrances, protection is provided at the beginning of the central reservation on the motorway, and at motorway exits in the event of a loss of vehicle control [6]. At motorway exits, this will primarily consist of semi-open, Y-shaped impact attenuators.

2. Energy dissipation by vehicle design

Today, engineers are designing vehicles to optimize kinetic energy absorption by incorporating crumple zones that absorb it during an accident. These parts of the vehicle are called crumple zones. Their role is to absorb kinetic energy during a frontal or rear-end collision.

2.1. Crumple zones

A car's crumple zones are components designed by engineers to absorb kinetic energy in the event of an accident. In other words, they are designed to absorb energy during a collision. Engineers design them to deform, thus absorbing the kinetic energy that could injure or even kill the vehicle's occupants. These zones are therefore essential for saving lives in the event of a road accident.

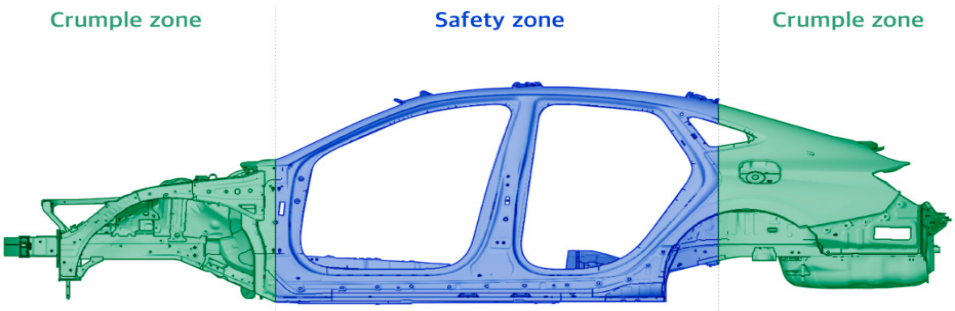

Figure 1. Reinforcement of the passenger compartment [7]

Regarding the passenger compartment, engineers have reinforced it to better protect occupants by minimizing deformation in the event of a road accident.

The reinforcement of this area has been refined over the years through the analysis of accident data, allowing engineers to design safer passenger compartments by carefully reinforcing specific design elements.

2.2. Reinforcement of the passenger compartment

The first measure to ensure passenger safety is to reinforce the passenger compartment in first-generation vehicles. Engineers observed that the compartment's deformation caused injuries and deaths among passengers. Indeed, in an accident, whether a head-on collision or a rollover, it is the passengers who absorb the vehicle's kinetic energy. This is what motivated the initial reinforcement of the passenger compartment in first-generation vehicles. In this first generation, the focus is solely on reinforcing the frames around the vehicle doors, see Figure 2.

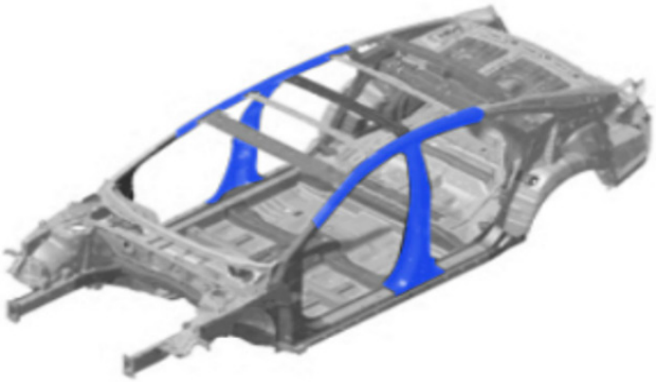

Figure 2. Passenger compartment reinforcement – 1st generation [7]

In the second generation, thanks to the analysis of accident data from hospitals and road safety authorities, engineers gathered enough information to further optimize the vehicle's passenger compartment. The focus here is on reinforcing the front of the cabin to prevent the legs of front passengers from being trapped in the bodywork in the event of hood deformation during a frontal impact (Figure 3).

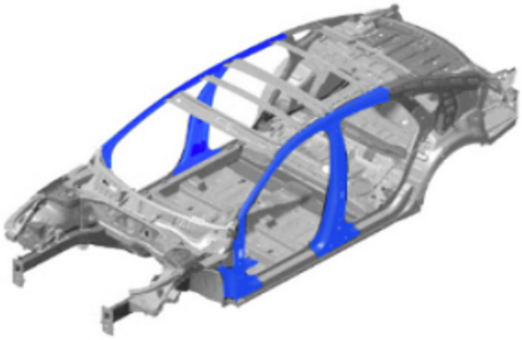

Figure 3. Passenger compartment reinforcement – 2nd generation [7]

For the third generation of passenger compartment design, engineers have gained sufficient experience identifying key areas requiring reinforcement. Furthermore, a better understanding of construction materials has allowed for the selection of the most suitable options. In this generation, knowledge gained from advances in computation and computer simulation has enabled more refined and safer designs, with components undergoing a series of virtual tests (Figure 4).

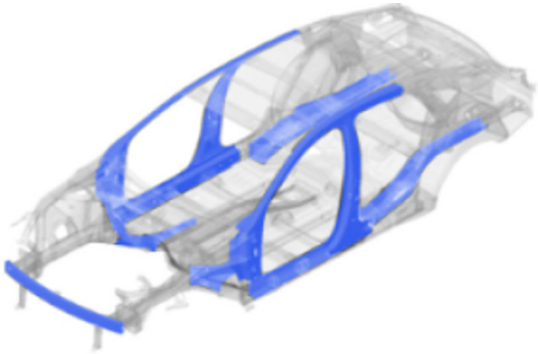

Figure 4. Passenger compartment reinforcement – 3rd generation [7]

2.3. Interior safety devices

In vehicles, it is important to note that measures are also taken to absorb passengers' kinetic energy and protect them from frontal and side impacts that could result in serious or even fatal injuries. These measures include seat belts, airbags, and headrests. These two systems, as shown in Figure 5, work together to progressively slow occupants' movement, absorbing and dissipating the kinetic energy generated during a collision, thereby improving overall safety.

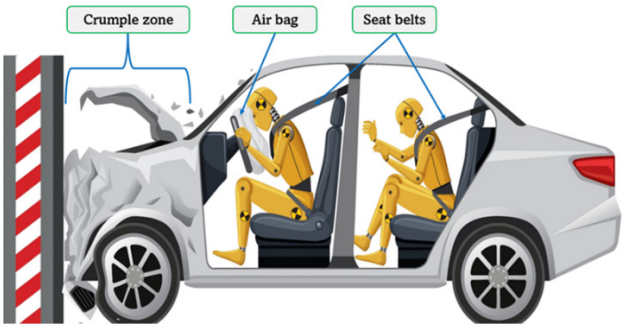

Figure 5. Safety devices in the vehicle [8]

Most people pay little attention to headrests when getting into a car, let alone consider them a safety feature. Yet, headrests do more than just improve rear visibility and provide comfortable head support; they play a vital role in protecting the head and neck in the event of an accident and help prevent injuries such as whiplash. People can experience severe crashes with no neck injury if there is little or no movement of the head relative to the torso (Figure 6).

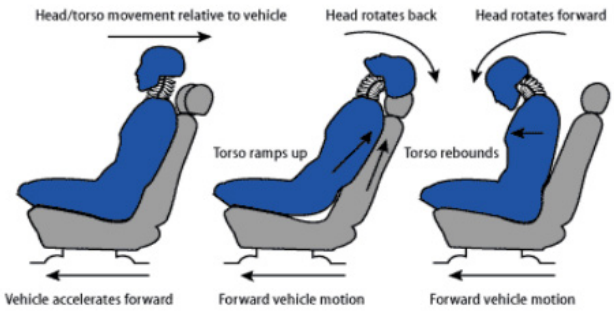

Figure 6. Head behavior during different movements of a moving vehicle [9]

For young passengers, especially babies and toddlers, car seats or booster seats with special seat belts play a crucial role in absorbing and distributing collision energy (Figure 7). These car seats are designed to securely hold infants and absorb and distribute impact forces across the strongest parts of their bodies, primarily the shoulders and hips. This helps prevent serious injuries by minimizing the concentration of impact energy and reducing the risk of ejection or contact with the vehicle's hard surfaces. When used correctly, car seats, in conjunction with seat belts, significantly increase the chances of survival and reduce the severity of injuries to young passengers in a collision.

Figure 7. Seat as an energy-absorbing device for young passengers/babies [10]

It is important to note that standard seat belts are not designed for infants. Therefore, it is necessary to use properly installed car seats or booster seats compatible with the vehicle's seat belt system to protect young passengers.

3. Energy dissipation by road safety guardrails

As we have already mentioned, absorbing kinetic energy is crucial for saving lives on the road in the event of an accident. This is why engineers design guardrails to prevent serious injuries and fatalities in road accidents. These guardrails, installed along the roadside or in the median strip of highways, deform by absorbing the vehicle's kinetic energy upon impact.

3.1. Road safety guardrails

Safety barriers are devices installed at the roadside or on the central reservation to reduce the impact of road accidents on the passengers involved. They come in various shapes and are made from a range of materials, including steel, wood, cables, and plastic. There are also models that combine wood and steel. Before being installed on the roadway, they must undergo crash tests in accordance with the European standard EN 1317 to be approved for use in European countries. These tests are carried out by independent crash-testing centers recognized and certified by the road authorities.

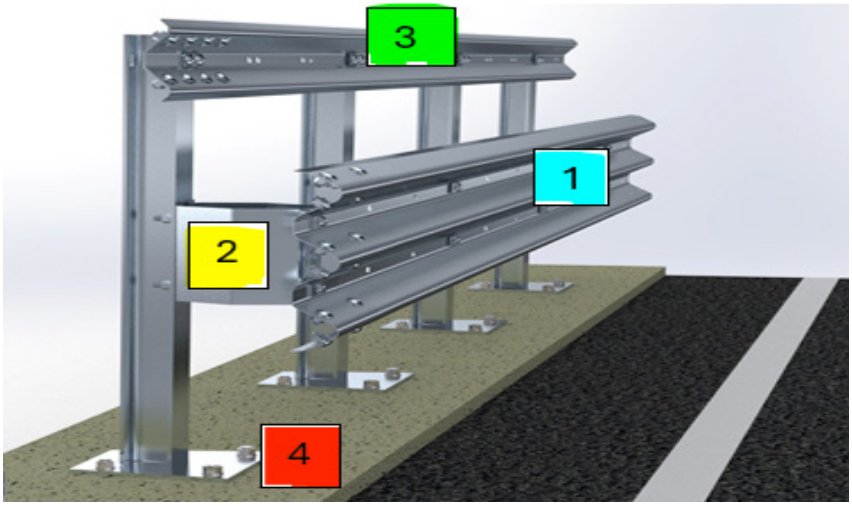

Figure 8. The 4-step energy absorption by the guardrail impact

The barrier illustrated in Figure 8 absorbs kinetic energy in four stages:

- The triple-wave bar (1) is impacted and absorbs some of the kinetic energy.
- If the vehicle is not stopped or diverted onto the roadway, the spreader bar (2) is activated; it deforms while absorbing kinetic energy.
- If the vehicle continues to impact the barrier, the double-wave bar (3) comes in action to absorb the remaining energy.
- If these first three elements fail, the ground anchor bolts are activated. This barrier has a high containment level (H4B). The anchor bolts will only be stressed in the event of a collision with a heavily loaded truck or bus.

3.2. Crash cushion

A crash cushion is a safety device designed to absorb a vehicle's kinetic energy during a collision, reducing the risk of passenger injuries and minimizing damage to vehicles and road infrastructure. Placed at the ends of guardrails or in front of bridge posts or piers, they attenuate the vehicle's kinetic energy, thus mitigating the severity of accidents and saving lives.

Engineers use specific materials such as steel, plastic, or a combination of both to design the crash cushions. They use special materials that deform upon impact. This device is designed to slow vehicles after an impact, redirect them safely, and prevent them from hitting the primary obstacle protected by the crash cushion.

Crash cushions are mitigation systems installed in high-risk accident areas, such as two-way roads, highways with potential intersections, exit ramps, and construction sites, to protect workers and construction materials. As mentioned earlier, they are specifically designed to absorb the kinetic energy of a stationary vehicle upon impact, significantly reducing its speed and thus preventing fatal accidents, serious injuries, or even death to the occupants.

Parallel crash attenuators are typically mounted on rails or a single rail to guide retractable plates in the event of an impact or collision. Their selection is based on specific criteria defined by road safety authorities or the companies that manufacture these products.

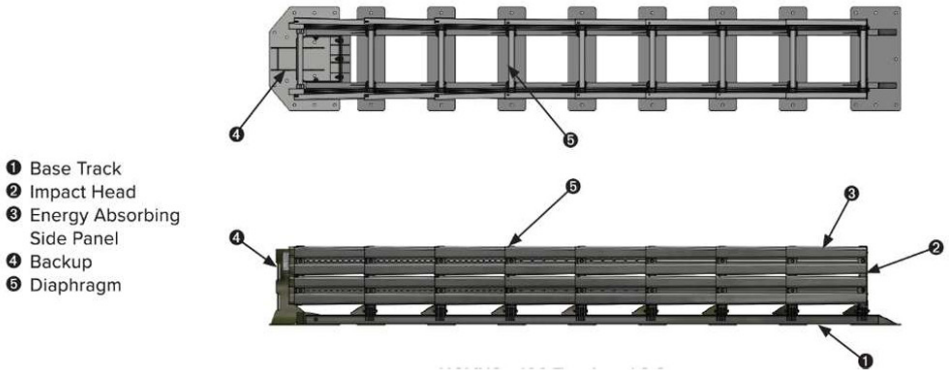

Figure 9. Parallel crash cushion [11]

The Y-shaped safety cushion functions exactly like a conventional steel airbag. It absorbs kinetic energy by retracting after impact. It is commonly found installed at highway exits to protect drivers who have lost control of their vehicle while exiting the highway.

Figure 10. Y-shaped crash cushion [12]

Trapezoidal crash attenuators are installed on high-speed roads, such as highways, at tunnel entrances, median barriers, or highway exits. However, their selection is reserved for road safety professionals or relevant road authorities. This type of attenuator is capable of absorbing very high kinetic energy, such as that of trucks. Its installation, therefore, requires technical expertise and must be performed by professionals. This is especially important because even a small error during installation can cause malfunction and, as a result, reduce protection for road users in case of an accident.

Figure 11. Trapezoidal road safety crash cushion [12]

4. Conclusion

Kinetic energy absorption systems are essential for saving lives on roads worldwide. Therefore, they must be installed correctly, whether they are internal vehicle devices, such as airbags and seat belts, or external devices, such as guardrails and impact attenuators.

References

1 European Union Road Federation. *EN 1317 – Overview of performance classes, ASI/THIV, and test parts.*

2 AASHTO. *Manual for Assessing Safety Hardware (MASH)*, 2nd edition, 2016.

3 Karkowski, M. "Correlations between road barrier parameters and ASI/THIV (EN 1317)." Roads and Bridges – Drogi i Mosty

4 Teng, T.-L., et al. Effect of W-beam post spacing and rail height on safety performance. *Advances in Mechanical Engineering* (2015).

5 Neves, R. R., et al. Performance of basic road barriers: ASI/THIV/PHD comparison of flexible vs. concrete. *J. Braz. Soc. Mech. Sci. Eng*. (2018).
6 Klugh, I., et al. *Energy Dissipated by Concrete Barriers in Vehicle Impact Scenarios* (KSU/KDOT Final Report, 2021).
7 Hyundai Motor Group. *The History of Crash Safety Technology*. Available at: https://www.hyundaimotorgroup.com/story/CONT0000000000072326
8 Munley Law. *Learn How the Crumple Zone Keeps You Safe in a Car Crash*. Available at: https://munley.com/how-the-crumple-zone-keeps-you-safe-in-a-car-crash/
9 Shelbourne Physiotherapy. Whiplash Treatment. Available at: https://physiotherapyvictoria.ca/icbc-whiplash-physiotherapy/whiplash-treatment/
10 Joie toddler & booster car seat. Available at: https://joiebaby.com/en/elevate-r129-toddler-and-booster-car-seat-2026
11 Barrier Systems Inc. Universal TAU-II-R Installation and Maintenance Manual. Available at: https://www.dot.ny.gov/main/business-center/engineering/specifications/appr-products/TAU-IIR_Iinstall_2_15_12v1.pdf
12 SMA Road Safety. Janus – Crash Cushion. Available at: https://www.smaroadsafety.com/en/c/crash-cushion/

Addresses:

- Ph.D. Student Fabrice Chatue, Babeș-Bolyai University, Faculty of Engineering, Piața Traian Vuia, nr. 1-4, 320085, Reşiţa, Romania f.chatue@laposte.net
- Prof. Gilbert-Rainer Gillich, Babeș-Bolyai University, Faculty of Engineering, Piața Traian Vuia, nr. 1-4, 320085, Reşiţa, Romania gilbert.gillich@ubbcluj.ro (**corresponding author*)
- Asist. Prof. Zeno-Iosif Praisach, Babeș-Bolyai University, Faculty of Engineering, Piața Traian Vuia, nr. 1-4, 320085, Reşiţa, Romania zeno.praisach@ubbcluj.ro
- Asist. Prof. Cristian Tufisi, Babeș-Bolyai University, Faculty of Engineering, Piața Traian Vuia, nr. 1-4, 320085, Reşiţa, Romania cristian.tufisi@ubbcluj.ro
- Assoc. Prof. Zoltan-Iosif Korka, Babeș-Bolyai University, Faculty of Engineering, Piața Traian Vuia, nr. 1-4, 320085, Reşiţa, Romania zoltan.korka@ubbcluj.ro

Table of content